Assessment of a Body Force Representation for Compressor Stability Estimation

by

Amish A. Patel

Submitted to the Department of Aeronautics and Astronautics
in partial fulfillment of the requirements for the degree of

Master of Science in Aeronautics and Astronautics

at the

MASSACHUSETTS INSTITUTE OF TECHNOLOGY

June 2009

Author .....
Department of Aeronautics and Astronautics
May 22, 2009

Certified by ....
Edward Greitzer
H.N. Slater Professor of Aeronautics and Astronautics
Thesis Supervisor

Certified by .....
Choon Sooi Tan
Senior Research Engineer
Thesis Supervisor

Accepted by .....
David L. Darmofal
Associate Department Head
Chair, Committee on Graduate Students

Assessment of a Body Force Representation for Compressor Stability Estimation

by

Amish A. Patel

Submitted to the Department of Aeronautics and Astronautics
on May 22, 2009, in partial fulfillment of the
requirements for the degree of
Master of Science in Aeronautics and Astronautics

Abstract

This thesis presents a methodology for the integration of blade row body forces, derived from axisymmetric and three-dimensional flow fields, for use in the stability analysis of axial compressors. The body force database represents the body forces as a function of the local flow coefficient times the overall flow coefficient; doing this overcomes a source of non-uniqueness in the representation. Stability calculations using body force databases from this methodology as well as from a legacy method, applied to axisymmetric streamline curvature calculations, are compared. A procedure for joining body forces extracted from axisymmetric and three-dimensional CFD calculations is presented along with an assessment of the sensitivity of the stall prediction and onset behavior to the shape of the body force curves. The slope of the body force curves near the point corresponding to peak pressure rise, as well as those near zero flow, are found to be important in determining the stall point and inception type. Comparisons to previous work and test data from a single stage research compressor are made.

Thesis Supervisor: Edward Greitzer
Title: H.N. Slater Professor of Aeronautics and Astronautics

Thesis Supervisor: Choon Sooi Tan
Title: Senior Research Engineer

Acknowledgments

I would first like to thank Mitsubishi Heavy Industries for not only funding my research and this project, but also providing bi-weekly input and feedback on my work.

I am grateful to Professor Greitzer and Dr. Tan, my thesis and research supervisors, for giving me the opportunity to participate in this project. Their patience, encouragement and valuable insights that they provided me on a weekly basis have only made me a better engineer and researcher, and I thank them for that. I am also equally indebted to Professor Spakovszky for his work on this project and his insight that he provided in our weekly meetings. I would also like to thank Dr. Adamczyk for his extremely productive visits and teleconferences, but most of all his patience, understanding and great conversations.

I would also like to thank all the other members of the MHI team I have been lucky to work with: Dr. Yifang Gong, Professor Quishi Li, Georg Reichstein, Jon Kerner, George Kiwada, and Johnathan Kerner. They were a constant source of ideas, support, and great friends and co-workers, without whom, this project and my work would not have been possible.

Finally I would like to thank my family for proving me with endless love and support from across the country, even when I didn't call as often as they'd like. This work is as much theirs as it is mine and I cant thank them enough for all they have done, past and present.

Contents

List of Figures

List of Tables

Nomenclature

r Radial location or direction

θ Circumferential location or direction

x Axial location or direction

P Pressure

V Velocity

U Local wheel speed

Ω Rotor rotational speed

ρ Density

$\phi_{local} = \frac{V_x}{U}$ Local flow coefficient

$\phi_{overall} = \frac{V_x}{U_{midspan}}$ Overall flow coefficient

$\phi\phi = \phi_{local}|\phi_{overall}|$ Phiphi reference variable

$\psi = \frac{P_{stator\,exit} - P_{t,\,IGV inlet}}{\rho\Omega^2 r^2_{midspan}}$ Compressor inlet total to exit static pressure rise coefficient (IGV inlet to stator Exit)

$\Phi_{local} = \frac{\phi_{local}}{\phi_{overall,\,design}}$ Normalized local flow coefficient (IGV inlet to stator Exit)

$\Phi_{overall} = \frac{\phi_{overall}}{\phi_{overall,\,design}}$ Normalized overall flow coefficient

$\Phi\Phi = \frac{\phi\phi}{\phi_{overall,\,design}}$ Normalized phiphi reference variable

$\Psi = \frac{\psi}{\psi_{design}}$ Normalized compressor pressure rise coefficient

F Axial transport flux variable or body force

G Circumferential transport flux variable

H Radial transport flux variable

S Source term

C Coefficient on second order term in polynomial

F_r Radial body force

F_t Tangential body force

F_x Axial body force

Chapter 1

Introduction

Gas turbine design procedures dictate that in order to ensure stable operation at all conditions a stall margin be included in setting the operating point of the engine. Current methods for determining the stall point rely on correlations of experimental data or computations based on simplified fluid dynamic models [2007, Longley]. Correlations require data from an actual compressor and are generally only applicable to compressors of similar geometry. Simplified flow models, while applicable to any input geometry, lack the ability to capture three dimensional effects that are known to be important to determining the type of stall inception and development of the final form of stall [1993, Day]. While accurate three-dimensional unsteady models exist, they require extensive computational time to capture those intra- and inter-blade row effects of the flow, which must be modeled to successfully determine the stall point and type of stall inception.

1.1 Background

1.1.1 Compressor Instability

A representative compressor performance map is shown in Figure 1-1, with pressure ratio (PR) plotted versus corrected mass flow for different corrected shaft speeds ($\frac{N}{\sqrt{\theta}}$). An operating line, defined as the line joining the expected operating points

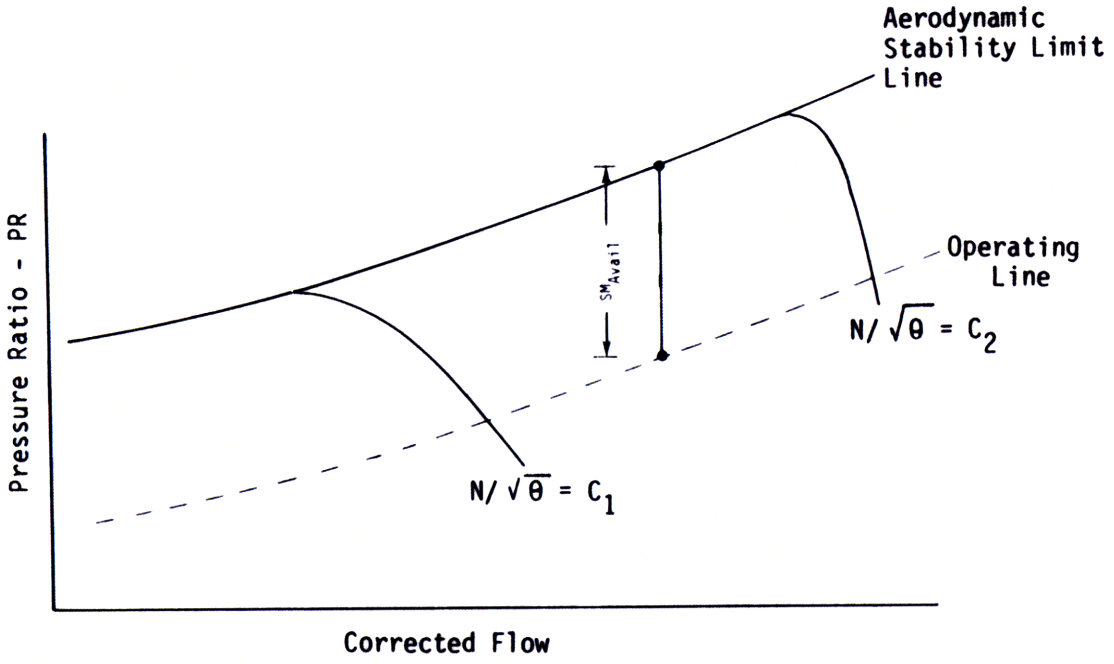

Figure 1-1: Example of a compressor performance map. The difference in pressure rise between the stall line and operating line at constant flow is often referred to as stall margin (SM_{Avail}) [1989, Steenken]

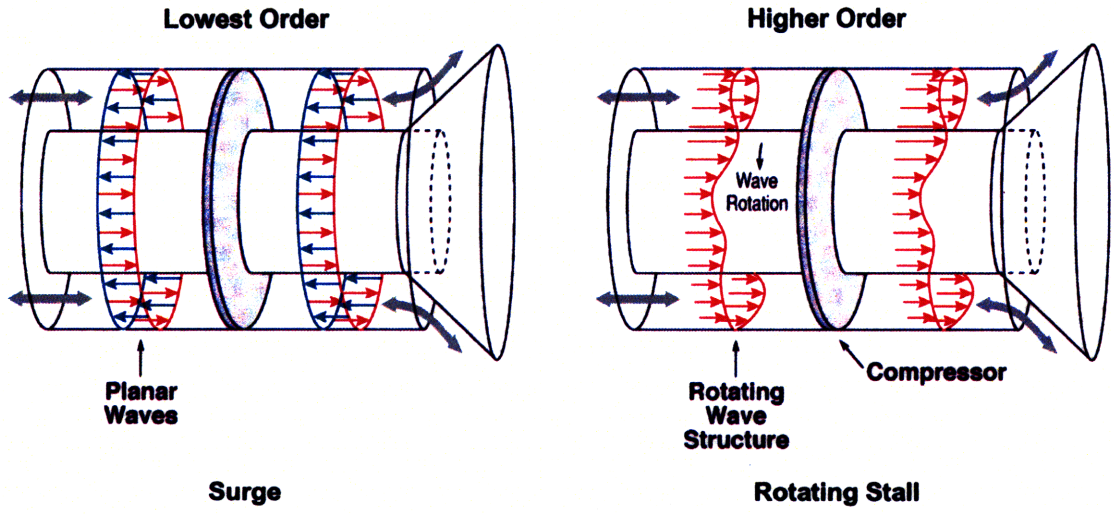

Figure 1-2: Sketch of the relation between the natural oscillatory modes of a compressor and stall type

of the compressor at each corrected shaft speed, and an aerodynamic stability line (or surge line) are shown. The difference in pressure rise between the operating line and the surge line at a constant corrected flow is often referred to as surge margin (although other definitions are also used [2004, Cumpsty]). For a given corrected shaft speed, the compressor exhibits an increase in pressure rise as the corrected mass flow is decreased. At a certain point, referred to as the stall point, further decrease in corrected mass flow leads to large amplitude flow oscillations and a drop in compressor pressure rise.

These oscillations are manifest in two forms, referred to as rotating stall and surge. Figure 1-2 shows a depiction of the natural oscillatory modes of a compressor and their relation to rotating stall and surge. Rotating stall can appear as either a single large, full span cell of low velocity flow or, as one or multiple part span stall cells [1999, Gong]. Surge is a one-dimensional oscillation of the flow through the entire compressor. This thesis addresses computations of the onset and routes to rotating stall.

1.1.2 Stall Inception

Two routes to rotating stall in axial compressors have been found, known as modal stall inception and spike inception [1998, Camp and Day]. Modal type stall inception is characterized by small amplitude disturbances with length scales comparable to the circumference of the compressor, and is also referred to as long wavelength inception. The growth of the disturbances in modal stall inception is initially an linear process occurring over multiple rotor revolutions [1998, Camp and Day]. Modal type disturbances typically rotate at between 20-50% of the rotor speed and include the entire length of the compressor.

Figure 1-3(a) shows an example of computed ϕ_{local} traces for a compressor stalling through long wavelength inception. The input disturbance (or forcing) results in a long wavelength velocity deficit which rotates around the annulus at roughly 40% of the rotor speed.

The second route to stall is through disturbances with length scales of a few blade

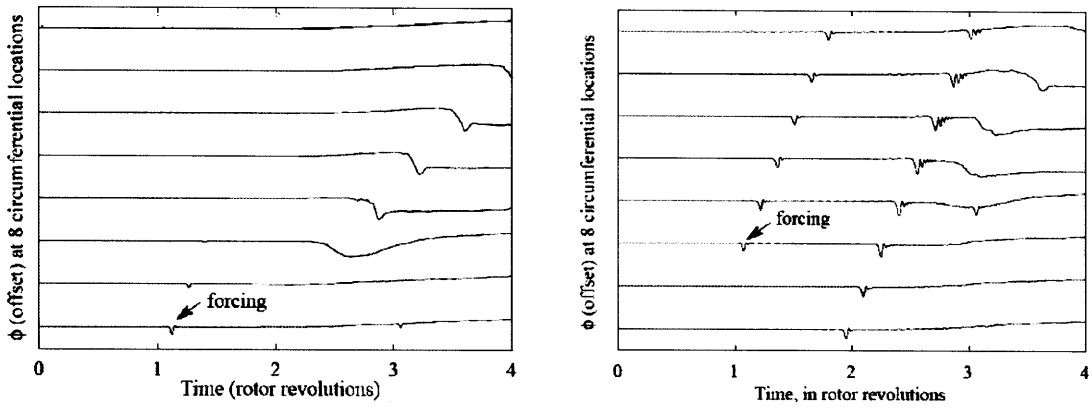

(a) Stall through long wavelength disturbances (modes)

(b) Stall through short wavelength disturbances (spikes)

Figure 1-3: Example of computed ϕ_{local} traces from the initial phases of compress stall through (a) long wavelength inception and (b) short wavelength inception [1999, Gong]

pitches and large amplitude. It is termed spike, or short wavelength, inception. Spike type inception is non-linear in nature and takes place on a time scale [1998, Camp and Day] that is shorter than long wavelength disturbances. In spike type stall inception an input spike grows into stall within 3-5 rotor revolutions. The disturbances have initial rotating speeds of roughly 70% of rotor speed [1999, Gong]. Figure 1-3(b) presents traces of computed ϕ_{local} for a compressor stalling through short wavelength inception. In contrast to the long wavelength stall inception depicted in Figure 1-3(a), the disturbance initially rotates at roughly 75% rotor speed and grows into a stall cell within two rotor revolutions.

Camp and Day gave a criterion for the occurrence of each type of stall inception based on the slope of the pressure rise curve near the stall point. Their results are shown in Figure 1-4. Stall points on the negative slope of the total-to-static characteristic, are associated with spike type. However, if the slope of the total-to-static pressure rise curve at stall onset is near the point of zero slope, the inception type is modal [1998, Camp and Day]. A complete stability prediction tool, the end goal of this project, would have the capability of predicting both short and long wavelength stall inception, as well as the compressor design features that lead to each.

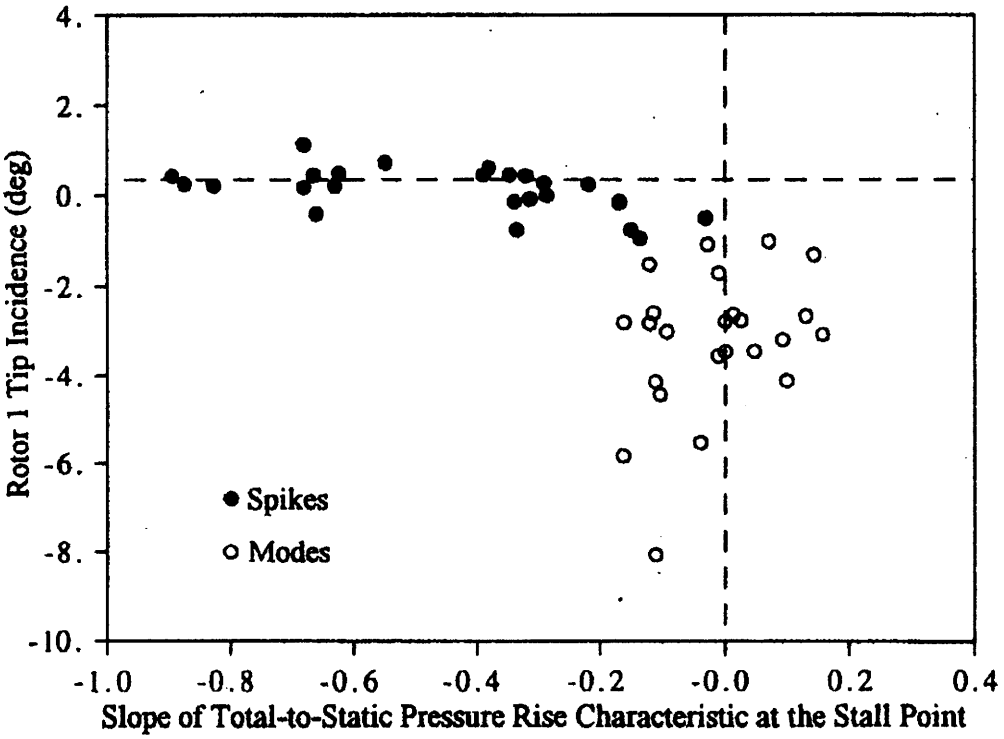

Figure 1-4: Data from Camp and Day [1998] showing a clear relation between the inception type and slope of the pressure rise curve near stall

1.1.3 Stability Calculations Using a Body Force Model

Accurate stability calculations require computation of the flow fields associated with an entire compressor system rather than a single individual blade row because not only the individual blade rows, but also their interaction with each other, must be examined. Gong [1999] showed that it is not necessary to describe the unsteady flow at a blade-to-blade level for stall inception, and that the blades can be smeared out and replaced by body forces. Replacing the blades effect on the flow with a body force, the computational cost and time of a simulation can be reduced.

Xu, Hynes, and Denton [2003] were able to capture long wavelength disturbances using a viscous body force model in combination with inviscid body forces from an axisymmetric flow field but the model lacked information regarding the distribution of the body forces. The body force model described in this thesis uses three dimensional computations to provide an improved description of short wavelength disturbances which are three-dimensional and localized to specific regions within a compressor.

1.1.4 Body Force Extraction and Database Generation

Kiwada [2008] developed a methodology for extracting body forces from three-dimensional Navier-Stokes calculations and from streamline curvature computations. A representative control volume used in the process is shown in Figure 1-5. For a calculation in which flow properties are calculated within a blade row, the control volume in Figure 1-5 would be further subdivided along the blade chord.

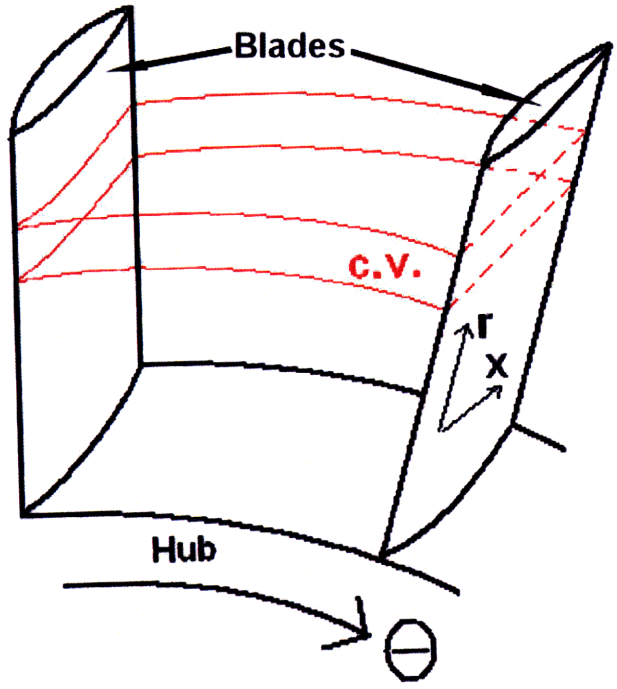

Figure 1-5: Example control volume for body force extraction [2008, Kiwada]

The body forces defined by Kiwada use a pitch average description of the flow. His blade force averaging method produces an axisymmetric force distribution by first averaging the flux terms, **F**, **G**, and **H**, defined in A.2, across the blade pitch and then extracting the body forces by equating the derivatives of **F**, **G**, and **H** to the source term, **S**, as in Eqn. A.4. Each flux variable is composed of four terms that appear in the equations for a force balance on a control volume. For example, the first term in **F** represents the axial mass flow, while the three remaining terms constitute the axial transport of momentum in the axial, radial and tangential directions, respectively. The flux terms are computed using a "blade force" average developed by Kiwada

[2008].

The blade force average expresses the flux from multiple points on a constant radial surface as the net average flux through the surface, thus enabling a three-dimensional flow field to be expressed as a pseudo-axisymmetric flow field, from which body forces can then be extracted. Combining body force distributions from different operating points allows one to generate a body force database that links the body forces for a given cell to local flow conditions, specifically the local axial flow coefficient, reported here as $\Phi_{local} = \frac{phi_{local}}{phi_{overall,design}}$.

1.2 Scope of the Thesis

1.2.1 Contribution

MIT is currently developing a procedure that capitalizes on recent advances in the understanding of compressor instability to provide a stall estimation tool which captures the stall point and the type of stall inception. Gong [1999] demonstrated the ability of a body force model to successfully capture both spike and modal type stall inception. In the implementation he used the body forces were prescribed by an input pressure rise characteristic and flow angles derived from experimental measurements rather than computed from knowledge of the blade geometry.

The stability model of Gong [1999] was based on a body force representation of the blade rows in which body forces are extracted from computed flow fields or experimental measurements, at operating points from reverse flow to design. Walker [2009] used this model to demonstrate spike type stall inception with a body force database extracted from axisymmetric streamline curvature flow fields using Kiwada's method. The streamline curvature body forces, however, lack information regarding the tip clearance effects, which are an important feature of the stall inception mechanism in the compressors of interest. This thesis addresses the issue of implementing body forces based on three-dimensional computations to resolve this point. The thesis also assesses the sensitivity of the stability simulation to the assumptions made and

the unknowns in the process.

1.2.2 Organization

The focus of the thesis is on incorporating body forces from streamline curvature and three dimensional CFD calculations into the stability calculation. Chapters 2-3 discuss the body force databases and presents a new procedure that redefines the body force database for use with three dimensional CFD derived body forces. Chapter 4 describes a method for the smooth joining of these body forces to those extracted from the streamline curvature results. An initial sensitivity analysis of the stability prediction tool as a whole is presented in Chapter 5.

Chapter 2

Technical Approach for Stability Analysis

2.1 Requirements of the Body Force Database

The requirements of the body force database are that it provides information over a range of flows from unstalled to possibly reverse flow. The reason is seen in Figure 2-1 which portrays how flow disturbance amplitude affects the range of the characteristic which is accessed. For spike type stall, which is characterized by large amplitude disturbances, the characteristic far from the peak pressure rise can be accessed even if the overall operating point is on the negatively sloped portion of the characteristic. Since stall can be characterized by low and even reverse flow in the region of the stall cell, a robust model must be able to locally respond to and describe conditions from design to reverse flow. This chapter discusses the CFD codes from which the body forces were extracted.

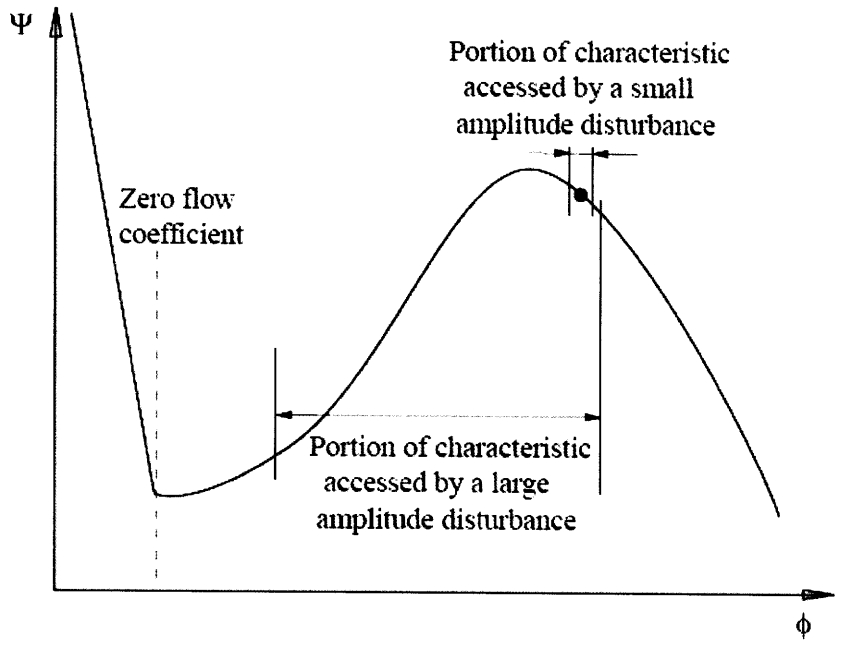

Figure 2-1: The effects of different disturbance amplitude on portion of characteristic accessed [1999]

2.2 CFD Codes

2.2.1 Streamline Curvature Code

The axisymmetric streamline curvature code used in this project was SIMSLEQ-07 provided by Denton [2007]. The streamline curvature code solves for the positions of the streamlines using radial equilibrium and mass conservation. The inputs required are loss and exit flow angles for each blade and vane row. The code is able to provide flow fields from the design flow coefficient, up to and past the stall flow coefficient, but there are several caveats. The code does not incorporate a model for tip clearance. It also has an internal limiter which prevents the velocity at any point within the flow from falling below 5% of the midspan value at that location. As such, regions of near zero and reverse flow, such as those in a tip gap or separated region are not well simulated, especially when the code is used far from the region of operating conditions for which it was designed.

The streamline curvature procedure also does not contain information within a blade row. To populate the body force database within a blade the total body force

(i.e. pressure rise) across a blade is extracted for each streamtube and then distributed within the blade using normalized axial force distributions generated by two-dimensional cascade calculations, computed using Fluent, at each radii (see Walker [2009] for more details). These two-dimensional cascade calculations also provide the input for loss and flow angle used in the code.

2.2.2 TBLOCK: Three-Dimensional Unsteady Navier-Stokes Solver

The three-dimensional calculations were from the TBLOCK v7.5 code, also provided by Denton [2007]. TBLOCK is a multi block, unsteady Navier-Stokes solver for multi-blade path flows. The input is compressor geometry, including tip clearances, inlet stagnation pressure, inlet temperature profiles, inlet flow angles and exit static pressure. The operating point is set by specifying a back pressure. By specifying increasingly higher back pressures the compressor is throttled, until it reaches a computational stall point.

To provide a quasi-steady axisymmetric flow field needed for the body force extractions, the TBLOCK flow fields are blade force averaged in the theta direction, as described in Section 1.1.4, and time averaged. Blade force averaging leads to a loss of information, as discussed in Section 3.1.1, but is a necessary step to extracting the body forces. Kiwada's body force extraction code is used on this quasi-steady axisymmetric flow field to calculate the body forces.

Two TBLOCK data sets have been generated, one with 0.9% (of annulus height) tip clearance and one with a 2.9% tip clearance. In this thesis, only the latter tip clearance data is used. The MHI test compressor with a tip clearance of 2.9% stalled at $\Phi_{overall} = .77$, and the TBLOCK computations were available up to $\Phi_{overall} = .78$.

2.3 Body Forces at Zero and Reverse Flow

The lowest flow coefficient that can be achieved using the current simulation tools (SLC plus Fluent) is $\Phi_{overall} = .44$. To create body force data points at zero and reverse flow, the zero flow point is assumed to have F_x, F_r and F_t equal to zero, with a corresponding flow field that consists of $\Phi_{local} = 0$ everywhere within the grid. Note that Φ_{local} is the local flow coefficient for a given cell, $\phi_{local} = \frac{V_x}{U_{midspan}}$, divided by the overall flow at design for the compressor. This assumption is analyzed in Section 5.3 to determine its impact on stall inception to changes in the force at $\Phi_{overall} = 0$.

Gamache and Greitzer [1990] showed that in reverse flow, an axial compressor exhibits a pressure rise curve characterized by a strongly negative slope. As such, an axial force, $F_{reverse}$, was input to produce a steep negative slope of the force curves in the reverse flow region.

Chapter 3

Body Force Database from Three-Dimensional CFD

3.1 Double Values in the Computed TBLOCK Body Forces

The stability estimation tool used is the UnsComp code developed by Gong [1999]. UnsComp requires a unique definition of the body forces, F_x, F_r, and F_t at any local flow coefficient, Φ_{local}. The body forces extracted from the streamline curvature calculation provide a unique set of forces as a function of Φ_{local} and thus could be directly implemented into UnsComp. However the TBLOCK description, expressed in terms of Φ_{local}, is not single valued.

Figure 3-1 shows an example of the force curve for a cell in the rotor at 43% chord and 4% span. There are multiple values of force in the TBLOCK curve near $\Phi_{local} = 1.30$. The streamline curvature body force curve, for the same cell, shows no double values.

Figure 3-2 shows the computational grid used in UnsComp indicating where double values in the TBLOCK data occur. Red cells indicate where at least one double value occurs within that particular cell over all the operating conditions, while blue cells contain no double values. The double values appear to be associated with the

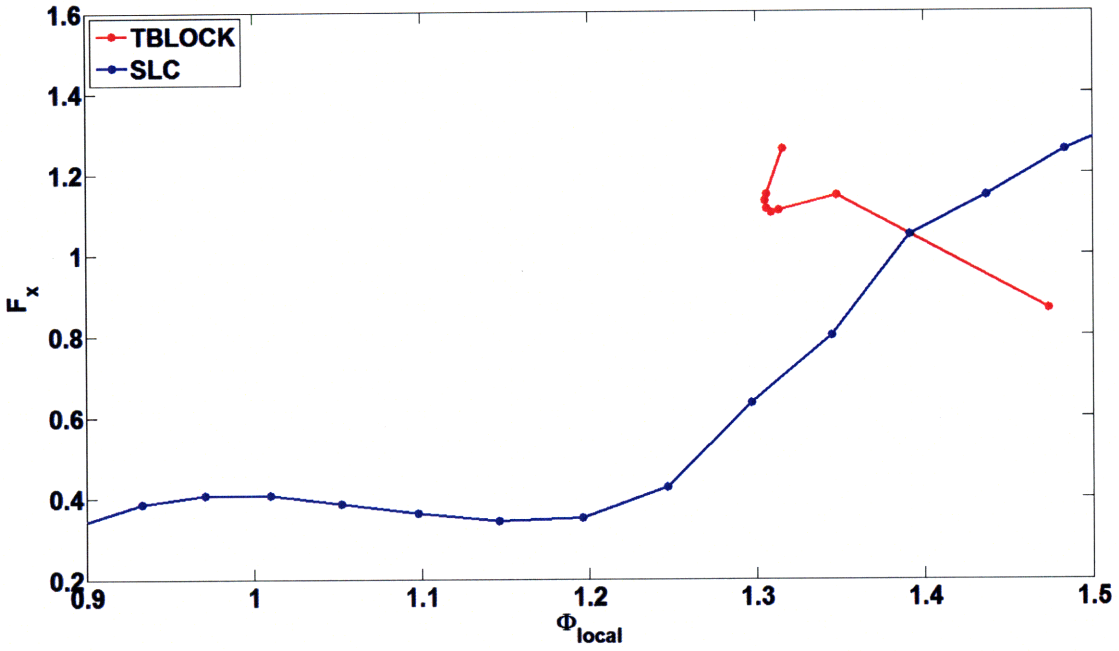

Figure 3-1: F_x vs. Φ_{local} comparison showing double values in TBLOCK body forces at Rotor, 43% chord, 4% Span

occurrence of reverse flow. For example the cluster of double values near the stator hub are caused by acceleration of the fluid in that region due to a combination of flow blockage from the tip leakage flow in the rotor and a small region of reverse flow along the stator hub. The area of reverse flow along the hub toward the trailing edge of the

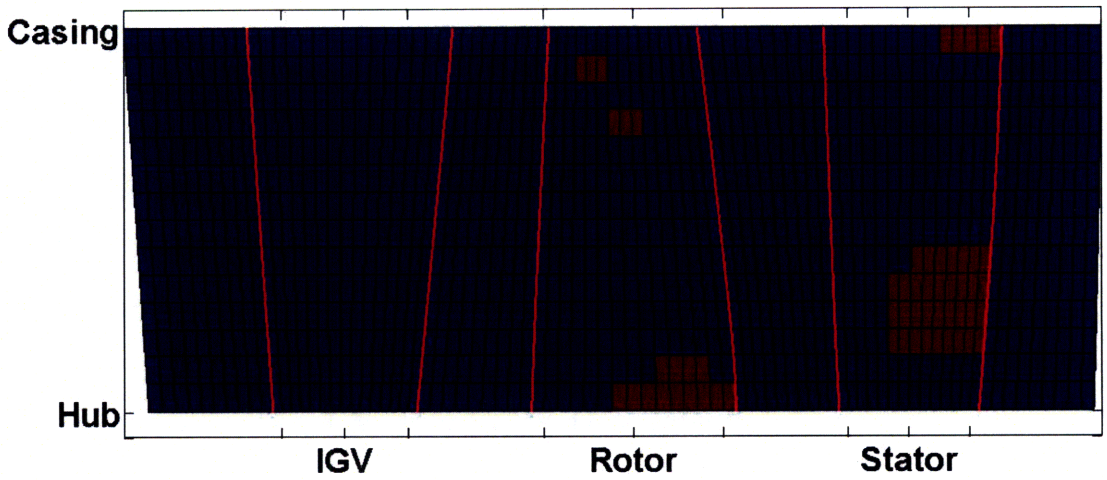

Figure 3-2: Cells containing double values in TBLOCK data when reference variable is Φ_{local}. Red indicates cells that contain double values, while blue indicates cells that contain no double values

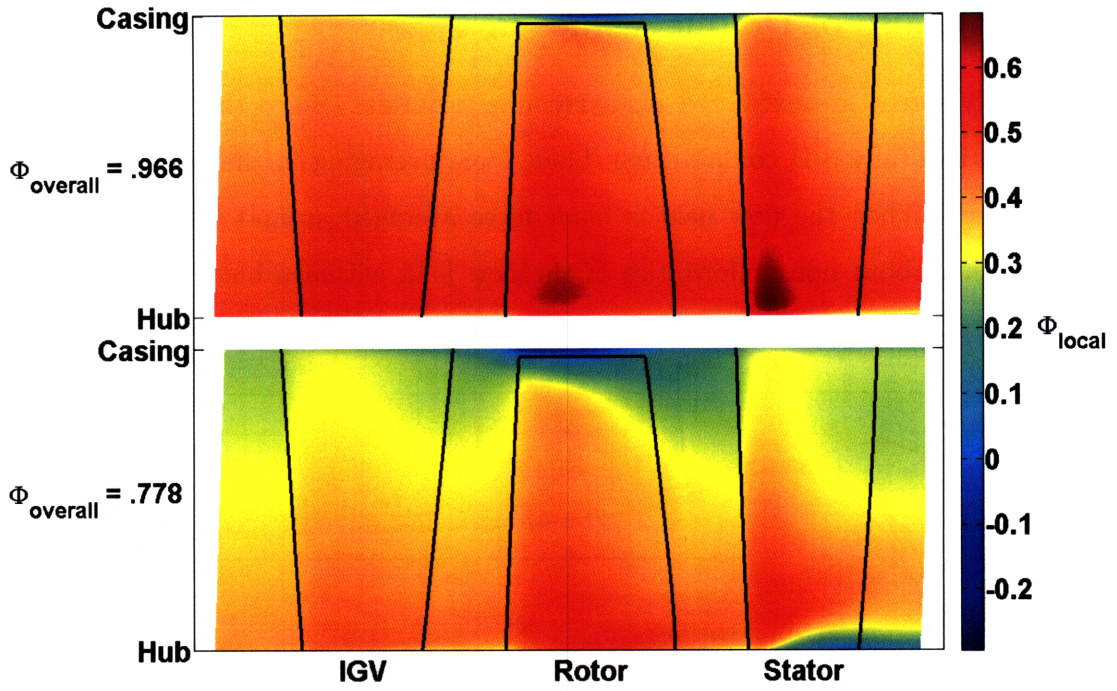

Figure 3-3: Pseudocolor plots of blade-force averaged values of Φ_{local} from TBLOCK near design ($\Phi_{overall} = .97$) and stall ($\Phi_{overall} = .78$)

stator, shown in Figure 3-3, causes a large upward shift of the streamlines resulting in a region of accelerated flow just above it, where the double values occur. As seen in Figure 3-3, the leakage flow from the tip of the rotor results in a high pressure region near the casing at the tip of the rotor. This high pressure region causes a downward shift in the streamlines within the rotor, leading to double values at trailing edge of the rotor on the hub. While the double values are most prevalent in regions of accelerated flow but they are also present in areas of reverse or low flow, as at the trailing edge of the stator tip where the flow is degraded due to the leakage flow from the tip of the rotor.

In summary, Figure 3-2 indicates double values in the stator hub and tip the rotor hub and tip. As mentioned, examination of the flow fields in these regions shows that they correspond to either areas of low flow or large streamline shifts due to low flow areas.

3.1.1 Cause of Double Values in Φ_{local}

The body forces are extracted on axisymmetric grids. Since the TBLOCK computation is a fully 3-D computation, blade-force averaging in the theta direction is performed. When the flow field is blade-force averaged around the circumference, information about non-uniformities of the flow field within a blade passage is lost, with the possibility that two flow fields could average to the same mean value.

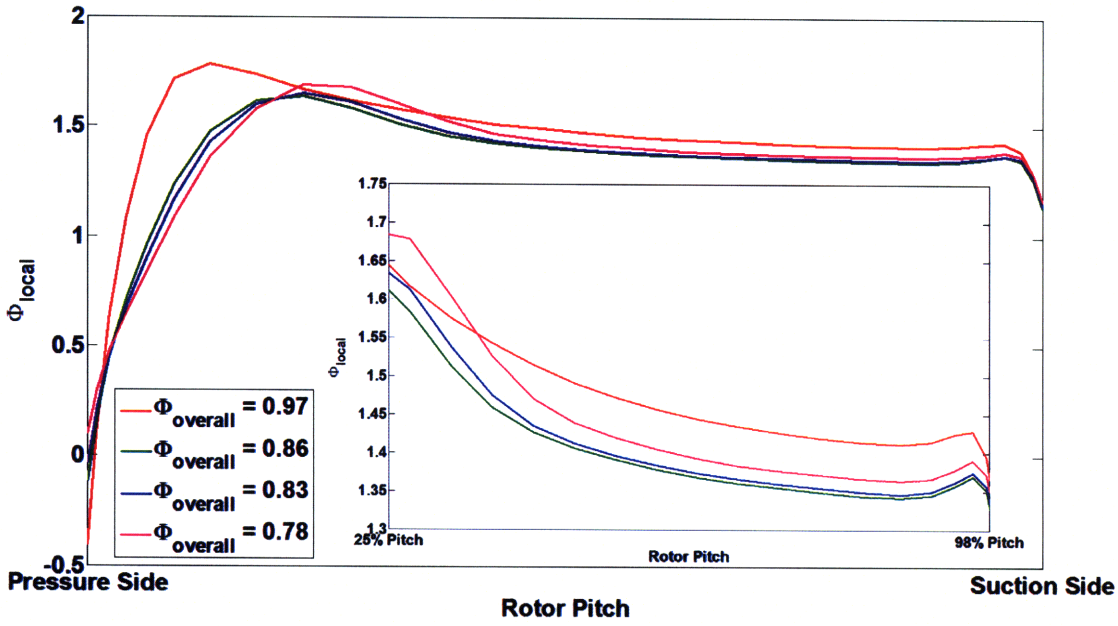

Figure 3-4: Profiles of Φ_{local} across rotor passage at various $\Phi_{overall}$

This situation is seen in Figure 3-4 which shows curves of Φ_{local}, at different $\Phi_{overall}$, across a rotor passage at 42% chord and 2% span. The inset figure is a zoomed in view. The majority of each velocity profile is characterized by almost a constant value of Φ_{local} from roughly 25% to 98% pitch. From the inset in Figure 3-4, as $\Phi_{overall}$ is decreased from design ($\Phi_{overall} = .97$) to $\Phi_{overall} = .86$, there is a decrease in Φ_{local}. However as $\Phi_{overall}$ is lowered further to $\Phi_{overall} = .83$, the Φ_{local} profile shows a higher average than the profile at $\Phi_{overall} = .86$, leading to a double value of Φ_{local}. When stall is reached at $\Phi_{overall} = .78$ the Φ_{local} profile is at a higher mean value than the other Φ_{local} profiles in the figure, except for $\Phi_{overall} = .97$.

Figure 3-5 shows $\Phi_{overall}$ versus Φ_{local} for a cell at 42% chord and 2% span in the

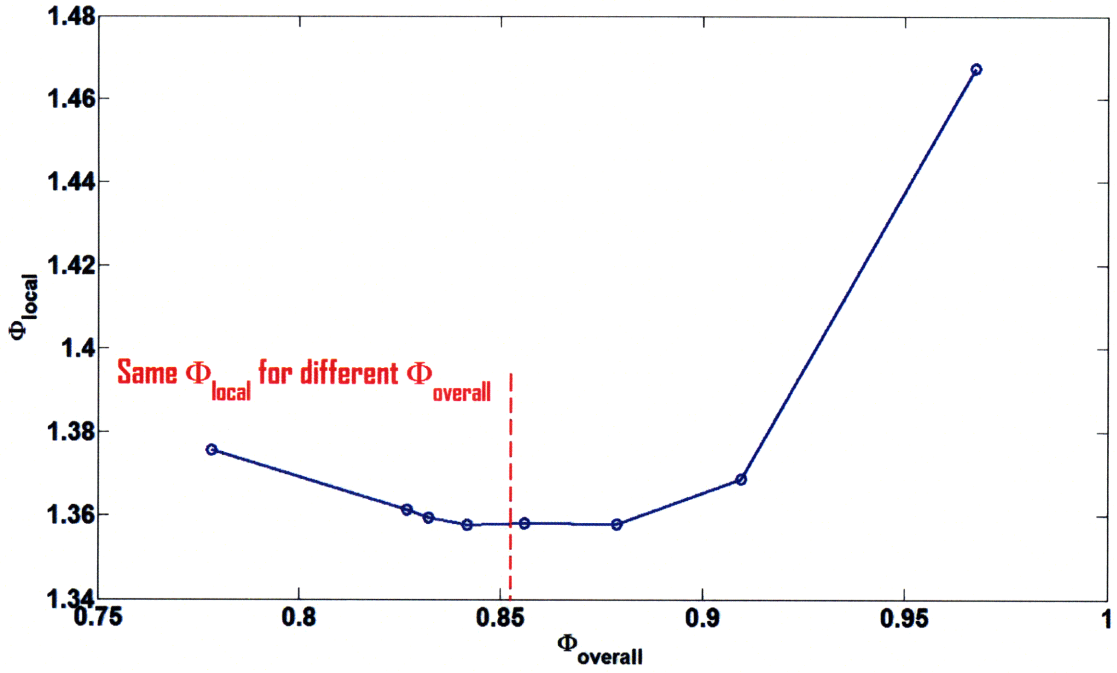

Figure 3-5: Blade-force averaged value of Φ_{local} vs $\Phi_{overall}$ for rotor passage

rotor after blade-force averaging has been performed. Double values in Φ_{local} as a function of $\Phi_{overall}$ can be seen.

A physical interpretation of the source of the double values is as follows. The initial decrease in the mean value of Φ_{local} across the passage is due to the decrease in mass flow as $\Phi_{overall}$ is decreased. Figure 3-3 shows how as the operating point is decreased from design towards stall, the tip leakage flow grows into a larger and larger region of low flow, which acts to block the incoming flow and cause a streamline shift towards the hub. The shift of the streamlines causes an acceleration of the inward flow, resulting in the Φ_{local} of cells near the hub doubling back to values of Φ_{local} seen at higher $\Phi_{overall}$.

3.2 Variable Change to Eliminate the Double Valued Behavior

The TBLOCK body forces can be used in the UnsComp stability code if the body force database is appropriately redefined to provide a unique definition of the body

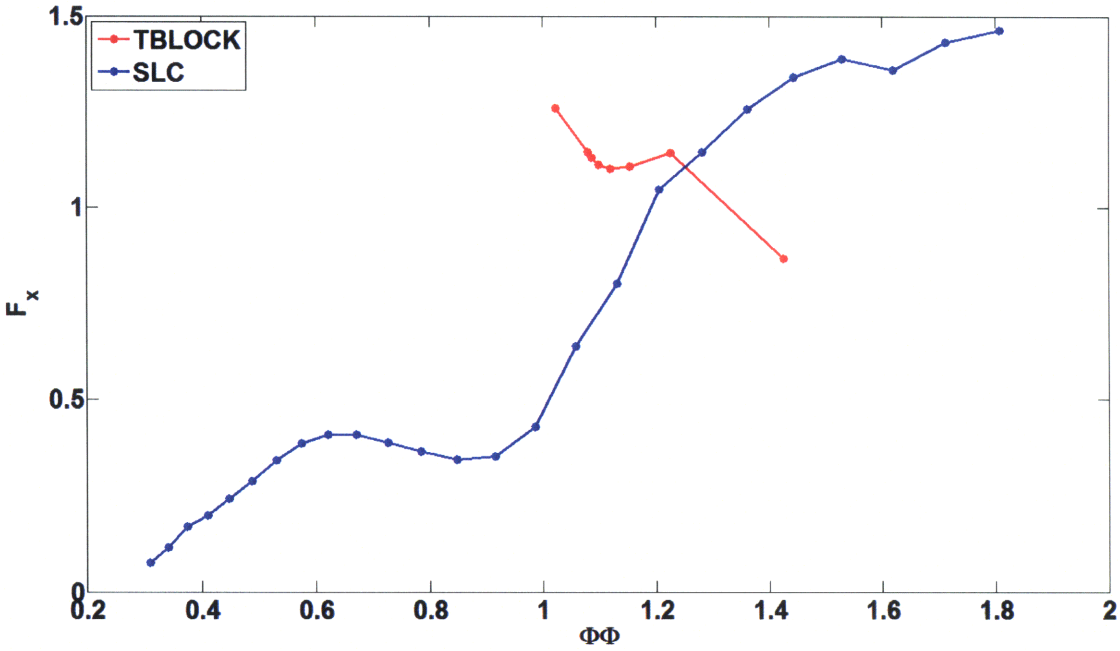

Figure 3-6: F_x vs. $\Phi\Phi$ at Rotor, 77% span, 42% chord showing elimination of double values with $\Phi\Phi$ reference variable

force at all local flow conditions. A new variable $\Phi\Phi = \Phi_{local}|\Phi_{overall}|$, was introduced to achieve this condition. Use of the $\Phi\Phi$ variable, while not completely eliminating the double values provides 86% reduction in the number of double values encountered for the grid used in this study, as well as a decrease in the severity of the double values.

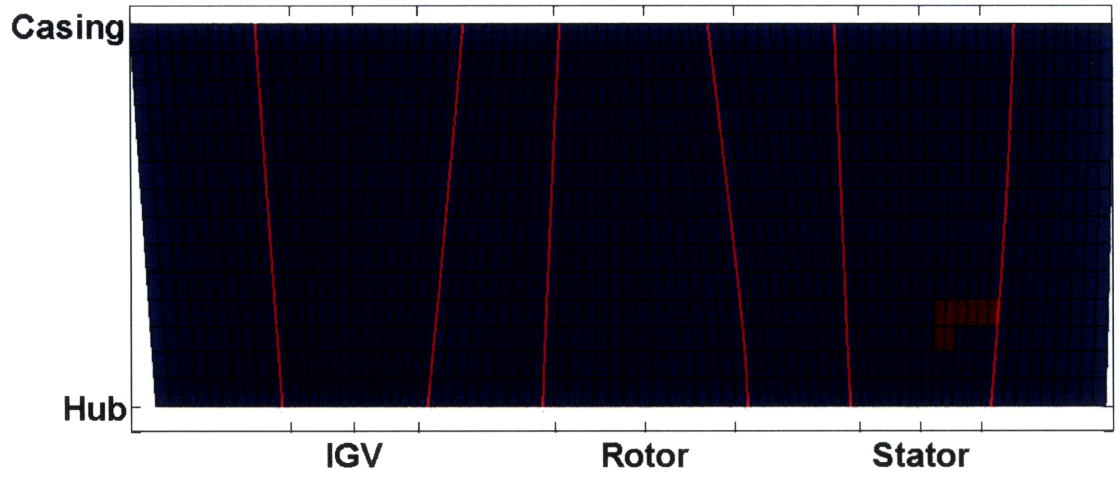

Figure 3-7: Cells containing double values in TBLOCK data when reference variable is $\Phi\Phi$. Red indicates cells that contain double values, while blue indicates cells that contain no double values

Figure 3-6 shows the analog to Figure 3-1 using the $\Phi\Phi$ reference variable. The plot shows how the redefinition of the reference variable stretches the body force curve along the abscissa and eliminates the double value that was present in the body force curve plotted in Figure 3-1. The body forces expressed as a function of $\Phi\Phi$ are now uniquely defined at all points along the curve.

Figure 3-7 shows the cells within the computational grid with a double value when the reference variable is $\Phi\Phi$. Comparing Figures 3-2 and 3-7, the change to the $\Phi\Phi$ reference variable gives a major reduction in the number of cells in which double values occur.

3.3 Assessment of $\Phi\Phi$ Performance as a Reference Variable

Assessment of the $\Phi\Phi$ reference variable was performed by comparing results of a stall simulation using a body force database generated from streamline curvature body forces and the $\Phi\Phi$ reference variable, with results of a stall simulation using the same values of body forces and the Φ_{local} reference variable.

The computed stall point when using the Φ_{local} reference variable is $\Phi_{overall} = .79$, as indicated by the green star in Figure 3-8, is 2.6% higher than the measured stall point. The Φ_{local} traces at stall, for twelve equally spaced circumferential stations at an axial location between the rotor exit and stator inlet are shown in Figure 3-9. The compressor stalls through spike type incpetion and the final form of stall is part span rotating stall, as depicted in Figure 3-10, which shows a pseudocolor plot of Φ_{local} for an $r - \theta$ plane between the rotor exit and stator inlet. The disturbance is input at one rotor revolution and initially rotates at 67% rotor speed. Three and one half rotor revolutions after the disturbance is input, the spike develops into a part span rotating stall cell which travels around the annulus at 52% rotor speed.

The computed stall point using the $\Phi\Phi$ reference variable is $\Phi_{overall} = .67$, as indicated by the cyan star in Figure 3-8, 13% lower than the measured stall point.

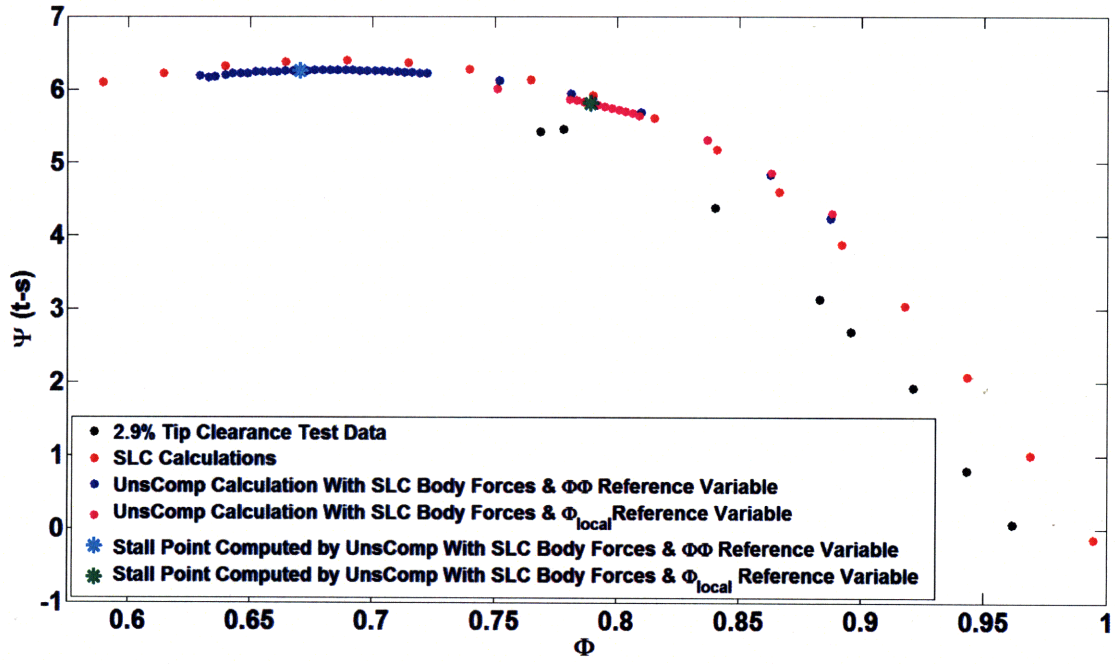

Figure 3-8: Comparison of pressure rise curves from test data, streamline curvature computations and, UnsComp calculations with streamline curvature body forces referenced to the Φ_{local} variable, in pink, and $\Phi\Phi$ variable, in blue. Green star indicates point at which UnsComp estimates stall using Φ_{local}, while the cyan star indicates where stall is calculated while using the $\Phi\Phi$ reference variable

The Φ_{local} traces at the stall point are shown in Figure 3-11, showing the compressor stalling through spike type stall inception, similar to the behavior observed when using the Φ_{local} variable. The initial rotating speed of the spike is 67% rotor speed while the stall cell rotates at 56% rotor speed. The final form of stall however is not part span stall as seen in the case when using the Φ_{local} variable, but rather ring stall as seen in Figure 3-12 which shows the pseudocolor plot of Φ_{local} at the rotor exit.

The $\Phi\Phi$ variable captures the same stall inception type as the Φ_{local} variable but the onset of stall is at a different flow coefficient. The reason for this is not know at present but suspected to be related to the behavior of the $\Phi\Phi$ variable near zero flow. When $\Phi_{overall} \neq= 0$, there are numerous distributions of Φ_{local}, and thus distributions of body forces, that can give rise to a flow field with a particular $\Phi_{overall}$; however, when $\Phi_{overall} = 0$, there is only one set of body force distributions available to choose from since $\Phi\Phi = 0$ when $\Phi_{overall} = 0$. The degree to which this behavior affects the

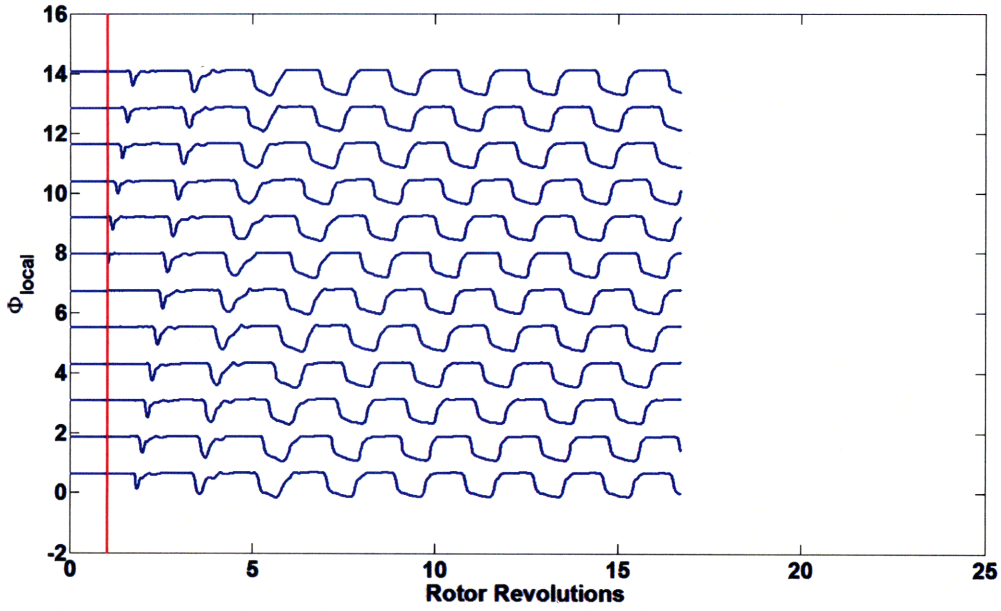

Figure 3-9: Φ_{local} traces at various circumferential positions at the casing for UnsComp with streamline curvature body forces and Φ_{local} reference variable at $\Phi_{overall} = .79$. Axial location between the rotor exit and stator inlet

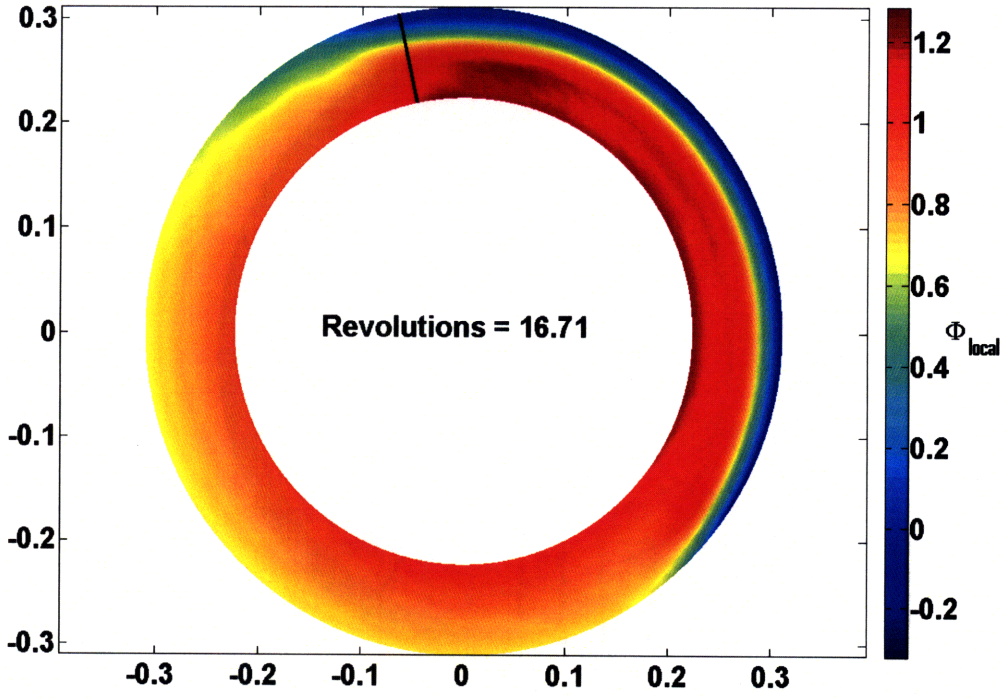

Figure 3-10: Pseudocolor plot of Φ_{local} showing part span stall cell in UnsComp calculation with streamline curvature body forces and Φ_{local} reference variable. Contour is at location between the rotor exit and stator inlet, for a $\Phi_{overall} = .79$, after the input of a spike type disturbance at 1 rotor revolution

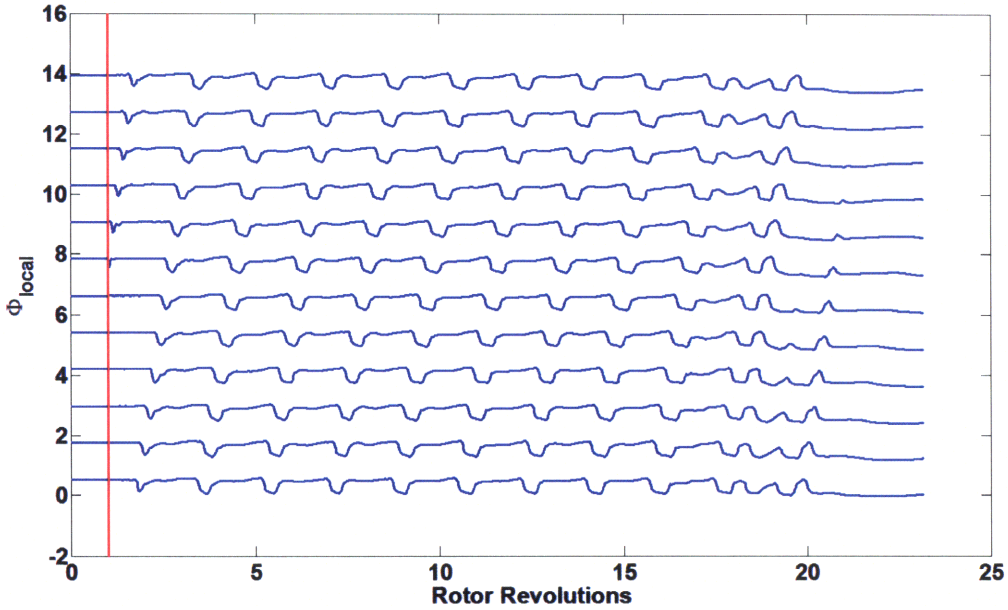

Figure 3-11: Φ_{local} traces at various circumferential positions at the casing for UnsComp with streamline curvature body forces and $\Phi\Phi$ reference variable at a $\Phi_{overall} = .67$. Axial location between the rotor trailing edge and stator leading edge

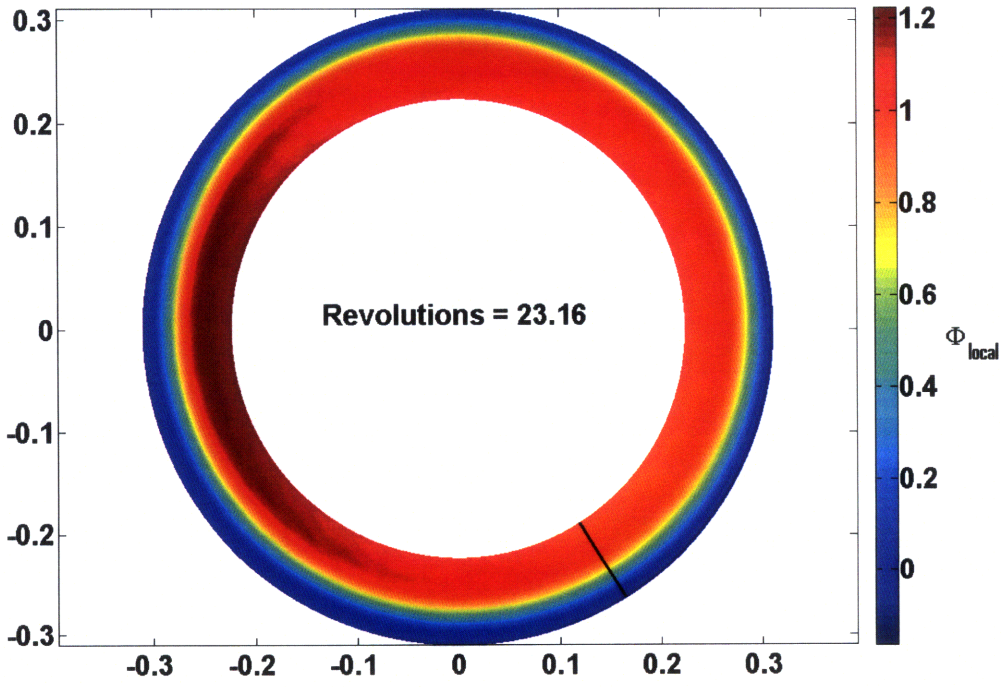

Figure 3-12: Pseudocolor plot of Φ_{local} showing part span stall cell in UnsComp calculation with streamline curvature body forces and $\Phi\Phi$ reference variable. Contour is at location between the rotor trailing edge and stator leading edge, for a $\Phi_{overall} = .67$, after the input of a spike type disturbance at 1 rotor revolution

stall simulation is the subject of ongoing investigation.

It is also not clear whether the simulation with the Φ_{local} reference variable would also exhibit ring stall if run for more rotor revolutions. The possibility remains the compressor, or simulation, may be prone to ring stall but is left for future investigation.

Chapter 4

Joining of SLC and TBLOCK Body Force Databases

4.1 Impetus for Joining the Body Force Databases

The TBLOCK body forces are used to give higher fidelity descriptions of the tip region flows for better estimates of the stall point and inception type. However, TBLOCK can only calculate flow fields up to the numerical stall point, while UnsComp requires that body forces be defined from design to reverse flow. Thus, the body forces derived from TBLOCK flow fields, from design to stall, must be joined to another descriptor from stall to low flow. The methodology used here is obtaining the body forces from streamline curvature plus two-dimensional viscous calculations. The overall body force description should yield curves which are smooth and continuous at all values of Φ_{local}.

4.2 Legacy Procedure For Joining the Databases

Walker [2009] proposed a procedure for joining the streamline curvature and TBLOCK body force databases based on a methodology developed by Kiwada [2008]. The aim was to provide a smooth joining of the integrated force values at each radii within the blade. The integrated force value is defined by $F_{x,integrated} = \int_{LE}^{TE} F_x dx$, from the

leading edge to trailing edge of a blade at a given radius.

TBLOCK provides flow fields and forces up to a numerical stall point, $\Phi_{overall,\,stall,\,TBLOCK}$. $F_{stall,\,TBLOCK}$ is the corresponding force for a given cell at that point. Given this point the corresponding streamline curvature body forces obtained at $\Phi_{overall}$ lower than $\Phi_{overall,\,stall,\,TBLOCK}$ are shifted in $\Phi_{overall}$ and force to match $\Phi_{overall,\,stall,\,TBLOCK}$ and $F_{stall,\,TBLOCK}$. This method provided a first approach to joining the TBLOCK and streamline curvature databases, but it was not tested with the stability code and did not result in smooth body force curves at all points within the computational domain.

With the procedure just described the body forces are matched between TBLOCK and streamline curvature where the two curves attach, but there is no constraint on matching the slope of the TBLOCK and streamline curvature body force curves. Walker [2009] notes that discontinuities in the slope of the resultant curve appear for body forces near the rotor tip. He also states that although the integrated force curves may match the value of force at this TBLOCK/streamline curvature joining point, when the force is distributed through the blade, discontinuities in force may appear for individual cells.

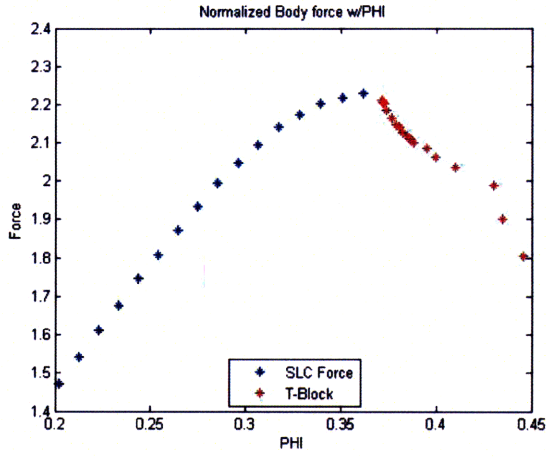

Figure 4-1: Example of an integrated force curve using the legacy method. Integrated forces are for the rotor midspan and plotted versus $\phi_{overall}$ [2009]

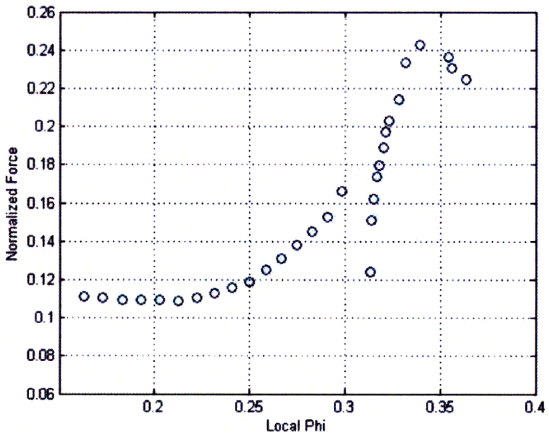

Figure 4-2: Example of a joined force curve for a local cell using the legacy method and showing a discontinuity in force. Forces are for a cell at the rotor 43% chord and 4% span, using the ϕ_{local} reference variable [2009]

Figure 4-1 shows a curve of the integrated body force versus Φ at the midspan of the rotor [2009]. It can be seen that the method provides a smooth joining of the integrated force curves at some radii. Figure 4-2 [2009], however, shows that discontinuities in slope and force appear for local cells upon redistribution of the forces.

4.3 A New Procedure for Joining the Databases

A procedure for joining the two databases was developed to avoid the local discontinuities encountered if only the integrated forces are matched. The procedure joins the streamline curvature and TBLOCK body forces on a local basis. At each cell within the computational grid, each force curve is defined over four regions of $\Phi\Phi$.

The four regions which play a different role in the fitting procedure and have different constraints are shown in Figure 4-3 for an example cell in the rotor at 31% span and 7% chord. They are: 1) TBLOCK Force Region, $\Phi\Phi \geq \Phi\Phi_3$; 2)Buffer region, $\Phi\Phi_2 \leq \Phi\Phi \leq \Phi\Phi_3$; 3) Streamline curvature fit region, $\Phi\Phi_1 \leq \Phi\Phi \leq \Phi\Phi_2$; 4)

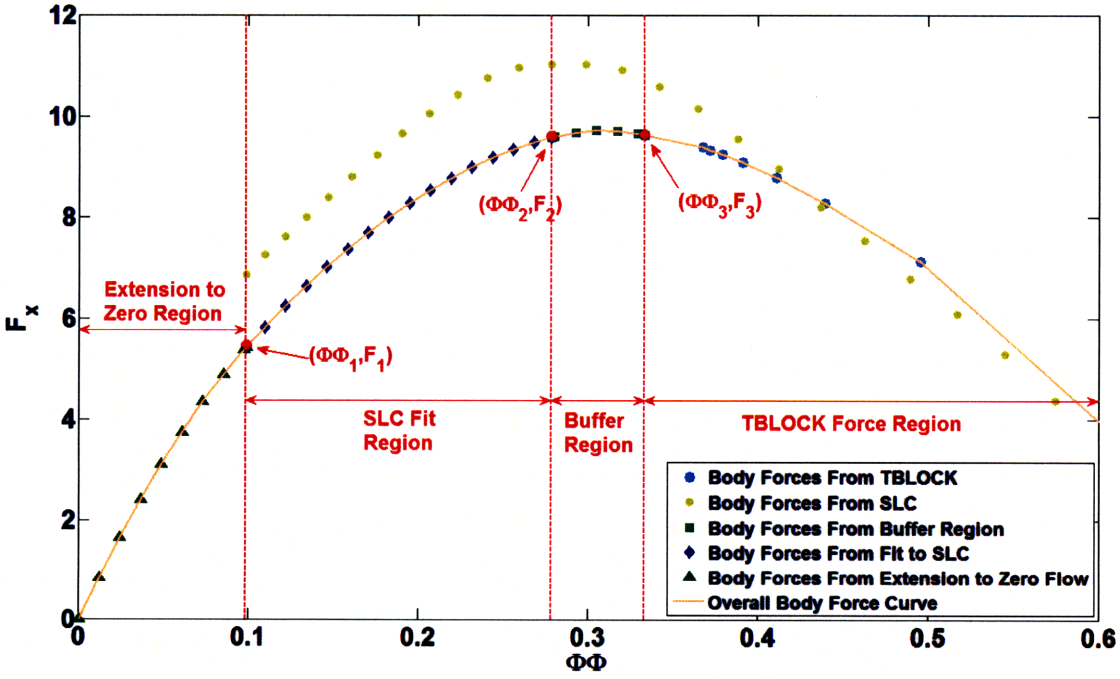

Figure 4-3: Example of F_x vs $\Phi\Phi$ body force curve in rotor at 31% span and 7% chord

Extension to zero, $0 < \Phi\Phi \leq \Phi\Phi_1$. The points $(\Phi\Phi_1, F_1)$ and $(\Phi\Phi_3, F_3)$ correspond to the lowest available streamline curvature and TBLOCK data points, respectively. The TBLOCK force region is not discussed in detail as the body forces in this region are the extracted TBLOCK body forces and remain unmodified.

Three desired characteristics of the resulting force curve drove the design of the fitting procedure. First, for $\Phi\Phi \geq \Phi\Phi_3$, the TBLOCK body forces are not modified since they are extracted from full three-dimensional calculations, and are considered the most accurate body forces currently available. Second, for $\Phi\Phi \leq \Phi\Phi_3$, the curve should be continuous and smooth with no discontinuities in either force or slope. Finally, although the streamline curvature body forces are not as accurate as the TBLOCK data, bulk information about the shape of the force curve can be used as a guide in extending the force curve for $\Phi\Phi \leq \Phi\Phi_3$. Doing this preserves the overall curvature of the data while avoiding discontinuities between the streamline curvature and TBLOCK body forces.

4.3.1 Buffer Region on $\Phi\Phi_2 \leq \Phi\Phi \leq \Phi\Phi_3$

The point $(\Phi\Phi_2, F_2)$ is determined by taking the first point in the streamline curvature data which is lower in $\Phi\Phi$ than the last available TBLOCK point, $\Phi\Phi_3$, and moving down in $\Phi\Phi$ space two data points in the streamline curvature data. The number of points moved down in $\Phi\Phi$ can be adjusted depending on the size of the step between the streamline curvature data. For the results presented here, the streamline curvature data had a spacing of $\Delta\Phi\Phi = .01$. If this operation results in only one, or zero, remaining streamline curvature data points, or there is no available streamline curvature data, the last TBLOCK point is connected to $\Phi\Phi = 0$ with a straight line, and no information from the streamline curvature data is used. The buffer region, plotted with green squares in Figure 4-3, is necessary to allow a smooth transition between the TBLOCK force curve and the portion of the force curve generated from the fit to the streamline curvature data. In the buffer region a second order polynomial is used with the constraints that the curve must pass through the point $(\Phi\Phi_3, F_3)$, as well as have the same slope as the TBLOCK data at that point. Additionally, at the

point $(\Phi\Phi_2, F_2)$, the buffer region and streamline curvature fit curves are matched to have the same value of force and slope.

4.3.2 SLC Fit Region on $\Phi\Phi_1 \leq \Phi\Phi \leq \Phi\Phi_2$

Two properties of the streamline curvature curves are used to constrain the generated body force curves for $\Phi\Phi \leq \Phi\Phi_2$ and $\Phi\Phi \geq \Phi\Phi_1$. As mentioned in Section 4.2, Camp and Day [1998] showed that the shape of the pressure rise curve (which is directly influenced by the shape of the force curves) is important in determining the stall inception point and type. Thus, to preserve the shape of the streamline curvature body forces, the first property used in the fit to the streamline curvature data was the coefficient of the second order term, C_{SLC}. Preservation of C_{SLC} ensures the concavity of the generated body force curve and the streamline curvature body forces is the same. The second property is the change in force from the beginning to the end of the fit, $\Delta F_{2-1,SLC} = F_{2,SLC} - F_{1,SLC}$, which ensures the local change in pressure rise from $\Phi\Phi_2$ to $\Phi\Phi_1$ is roughly conserved.

Once C_{SLC} and $\Delta F_{2-1,SLC}$ are determined for the curve from $\Phi\Phi_2$ to $\Phi\Phi_1$, a second order polynomial is defined which shares the same slope and value of force as the buffer region curve at $(\Phi\Phi_2, F_2)$, as well as the same slope and force value as the extension to zero at $(\Phi\Phi_1, F_1)$. Figure 4-3 shows how the curves fit together. The curve in blue diamonds mimics the shape and change in force of the streamline curvature body forces, yellow dots, but is shifted to match the buffer region and extension to zero.

4.3.3 Extension to Zero Flow on $0 < \Phi\Phi \leq \Phi\Phi_1$

The final two regions of flow to be defined are the extension to zero flow on $0 \leq \Phi\Phi \leq \Phi\Phi_1$ and the reverse flow region on $\Phi_{reverse} \leq \Phi\Phi \leq 0$. For the extension to zero flow, another second order polynomial is generated with the constraint that it must share the same slope and force value at $(\Phi\Phi_1, F_1)$. The extension to zero is plotted as green triangles in Figure 4-3. As mentioned in Section 2.3 an anchor point

at $(0, 0)$ is included in the body force database so the extension to zero curve passes through this point. In the reverse flow region, the body forces are defined by the reverse flow data point described in Section 2.3.

Figure 4-3 shows the force curves from streamline curvature and TBLOCK for a cell in the rotor at 31% span and 7% chord, as well as the resultant curve from applying the joining procedure to those force curves. Also marked are the different regions of the curve described in this section, which constitute the resultant body force curve. The resulting body force curve maximizes the use of TBLOCK body forces, preserves the shape of the streamline curvature body force curve and avoids discontinuities between streamline curvature and TBLOCK body forces.

Chapter 5

Sensitivity of the Stability Calculation to Shape of Force Curves

5.1 Motivation for the Sensitivity Study

Gong [2008] showed that variations in the shape of the pressure rise curve can lead to changes in both stall point and stall inception type. While the pressure rise in his formulation directly translates into the axial body force F_x, this is not true for a flow with radial non-uniformities in the background flow. It is not evident how changes to portions of the local body force curves past the peak are manifest as changes in the overall pressure rise curve, because the body force curves are defined in terms of local flow properties and combinations of local properties can give rise to similar overall flow properties. Thus, a study of the effects of changes to the body force curve past the peak was performed.

Initial attempts at using the joined body force database were unsuccessful at reproducing stall, and the number of assumptions and variables in the joining process and use of the TBLOCK data were deemed too numerous to analyze given the time frame of this thesis. A sensitivity analysis using streamline curvature body forces was

thus carried out.

Three aspects were examined. The first addressed changes to the slope of the force curves near the flow coefficient corresponding to the peak pressure rise, the second addressed changes to the force value at zero flow coefficient, and the third addressed changes to the slope of the reverse flow region of the body force curves. The studies aimed both to provide insight into how changes in the force curves effect the calculated stall point and inception type and to elucidate areas of importance in the joining procedure and limits for changes in those parameters, for which there was little or no guidance.

In the results presented here the baseline used for comparison is the UnsComp calculation using the $\Phi\Phi$ variable and streamline curvature data, presented in Section 3.3. This case (Figure 3-3) exhibited part span rotating stall through spike type inception at an overall flow coefficient of $\Phi_{stall,\,baseline} = .670$, with a final stall state of ring stall.

5.2 Sensitivity to Shape of the Force Curve Near the Peak

Gong [2008] found that variations in the slope of the pressure rise curve near the peak had the most impact on the stall point estimate. His results were based on the incompressible version of UnsComp in which the body forces were derived from a prescribed pressure rise curve. For the compressible version of UnsComp the body force curves themselves were modified to assess how changes in the body force curves past the peak pressure rise would affect the stall point estimate.

Table 5.1 lists the three cases examined while Figure 5-1 gives a graphical representation of example force curves from each case. For all three cases, each force curve was comprised of streamline curvature body forces for flows larger than $\Phi\Phi_{peak}$. Specifically the point ($\Phi\Phi_{peak}$,F_{peak}), the $\Phi\Phi$ and force value at $\Phi_{overall} = .78$ respectively, was connected by a straight line to a specific value of $F_{\Phi_{overall}=0}$, the force at

Case	$F_{\Phi_{overall}=0}$
1	0
2	F_{peak}
3	$\frac{F_{peak}}{2}$

Table 5.1: List of cases for changing shape of force curve near peak

$\Phi_{overall} = 0$. The slope of the reverse flow body force curve was unchanged in all four cases although the reverse flow curve was connected to the point at zero flow as seen in Figure 5-1. Case 1 had $F_{\Phi_{overall}=0} = 0$ similar to the way the baseline is joined to zero flow. Case 2 had $F_{\Phi_{overall}=0} = F_{peak}$, where F_{peak} is the value of force for a given cell at peak pressure rise. Case 2 results in a body force curve of zero slope from $\Phi\Phi_{peak}$ to zero flow, i.e. it represents a compressor which produces a constant pressure rise for flows below $\Phi\Phi_{peak}$. Case 3 had $F_{\Phi_{overall}=0} = \frac{F_{peak}}{2}$ giving a line of intermediate slope.

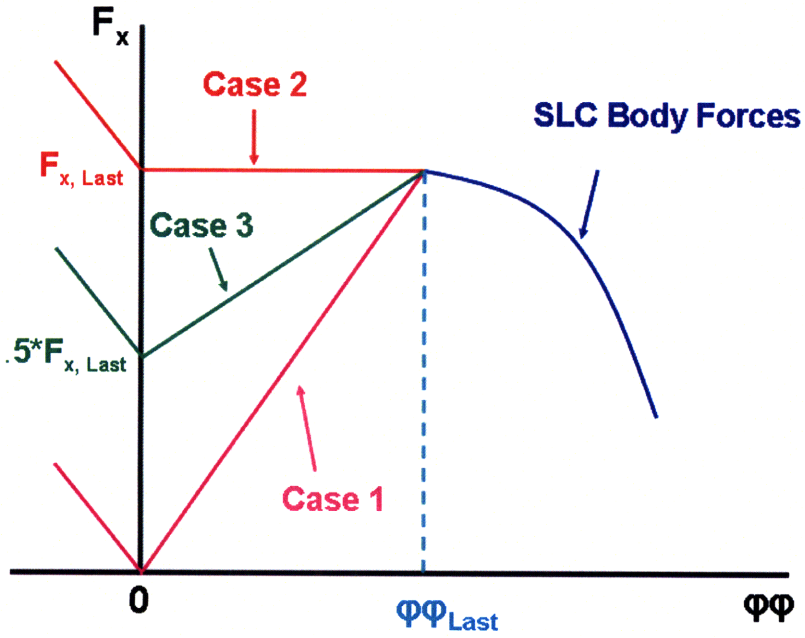

Figure 5-1: Graphical representation of force curves for three slope sensitivity test case studies

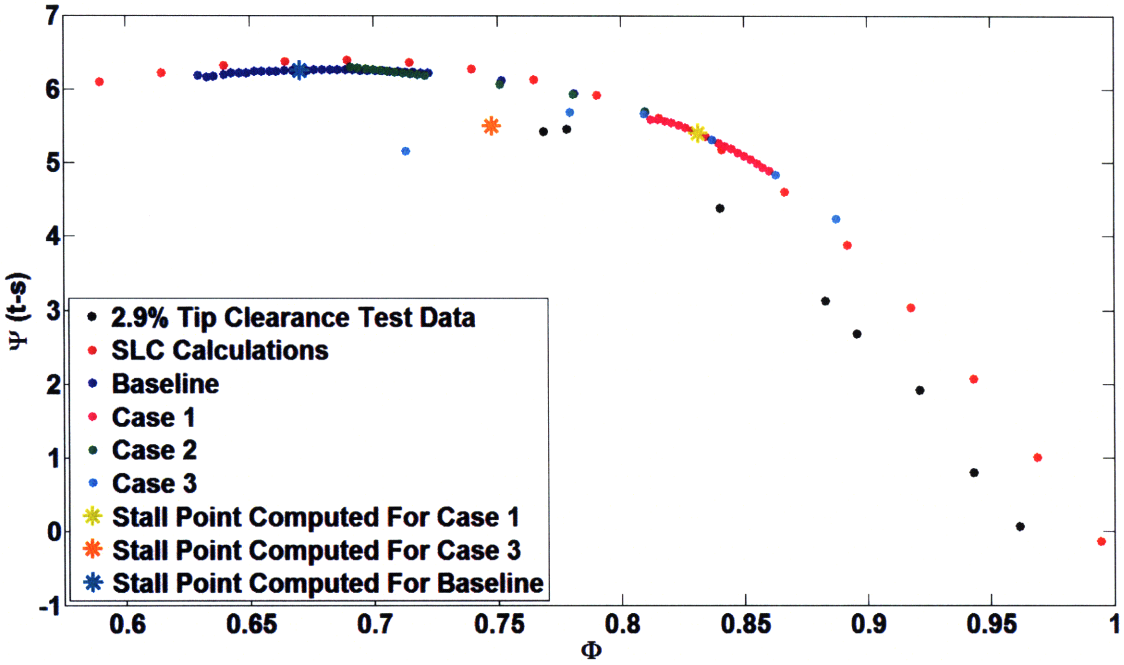

Figure 5-2: Total-to-static pressure rise curves for Cases 1-3

The resulting total-to-static pressure rise curves for Cases 1 to 3 are plotted in Figure 5-2, with the baseline included for reference. The data for each case is plotted up to the last flow coefficient at which UnsComp was able to calculate an axisymmetric flow without reverse flow. (The axisymmetric solutions are used to populate the initial flow fields of the three-dimensional calculations in UnsComp, and reverse flow can possibly predispose the simulation to stall.)

5.2.1 Case 1

The Φ_{local} traces for Case 1, in Figure 5-3, indicate stall through spike type stall inception leading to part span rotating stall at $\Phi_{overall} = .832$. Figure 5-4 shows the pseudocolor plot of Φ_{local} at the rotor exit including the part span rotating stall cell. The initial speed of the spike is 67% of rotor speed while the stall cell rotates at 43% rotor speed.

The slope of the total to static pressure rise curve for Case 1 is negative at the stall point and the stall inception type is a spike, which is in accord with the findings of Camp and Day [1998] presented in Section 1.1.2. In contrast to the baseline, Case

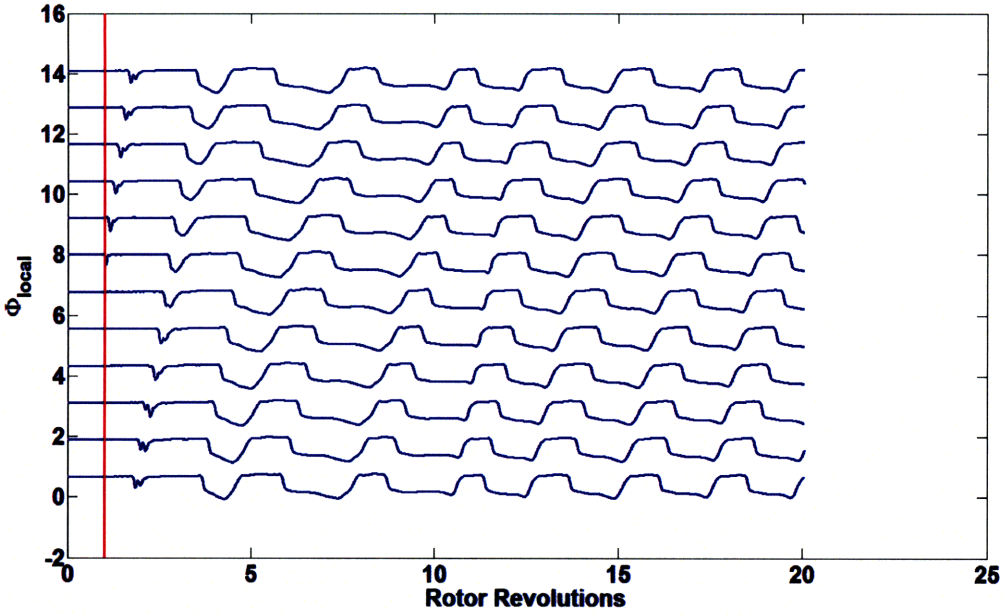

Figure 5-3: Traces of Φ_{local} for sensitivity Case 1 showing spike type stall inception at $\Phi_{overall} = .832$ leading to part span rotating stall

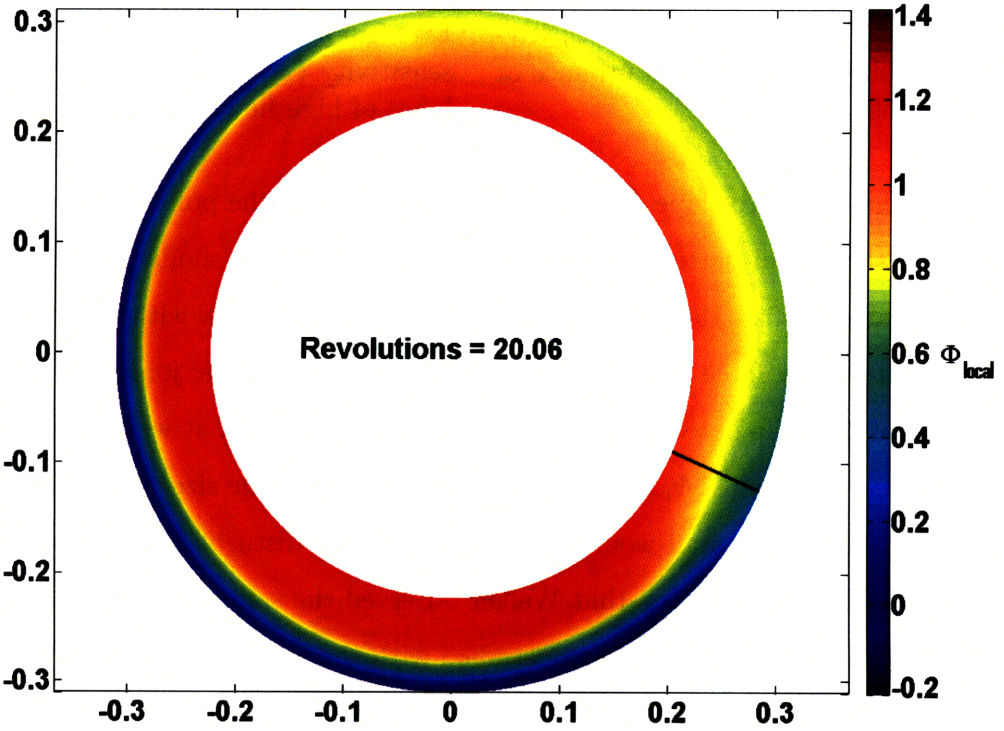

Figure 5-4: Pseudocolor plot of Φ_{local} for sensitivity Case 1 showing rotating part span stall cell at $\Phi_{overall} = .832$

1 does not go into ring stall.

5.2.2 Case 2

The Φ_{local} traces for Case 2 at $\Phi_{overall} = .691$ are shown in Figure 5-5. The final flow pattern, shown in Figure 5-6, is characterized by an eight lobed pattern of high flow regions that rotate around the annulus at 30% rotor speed. This appears to be a modal pattern which does not develop into large amplitude rotating stall.

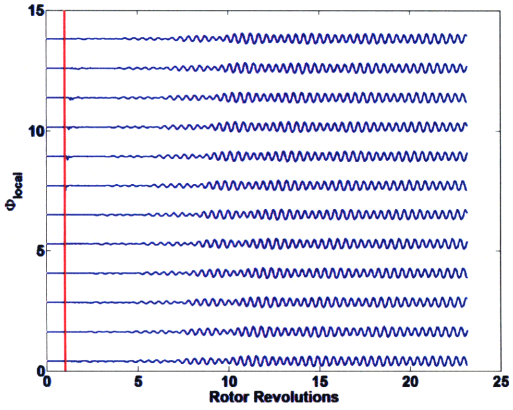

Figure 5-5: Traces of Φ_{local} for sensitivity Case 2 showing modal disturbance at $\Phi_{overall} = .691$

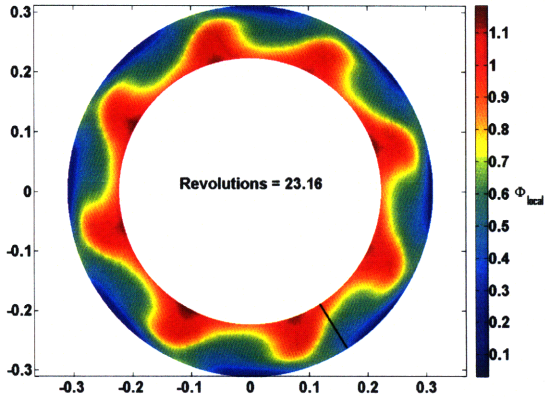

Figure 5-6: Pseudocolor plot of Φ_{local} for sensitivity Case 2 showing eight rotating lobes of high flow at $\Phi_{overall} = .691$

Given the near zero slope of the pressure rise curve at the points where the spike was input, the modal patterns observed bear resemblance to similar results encountered by Walker [2009]. He noted modal patterns within the flow with the full streamline curvature body force database and Φ_{local} reference variable, joined through zero force at zero flow. He noted that for the same operating point at which stall was observed in his simulations, $\Phi_{overall} = .78$, a disturbance $\frac{1}{100}$ the size of the disturbance that caused spike type stall would result in a rotating disturbance characterized by an eight lobed pattern. Given that Walker observed the same eight lobed pattern it is possible that the compressor being studied with the Case 2 body forces is modal.

The time traces of $\Phi_{overall}$ and Ψ (s-s) were examined for the perturbed case and are shown in Figure 5-7 (a) and (b), respectively. The modal pattern observed does not have a drop in pressure rise, but there is a change in both $\Phi_{overall}$ and Ψ (s-s)

which converge to steady average values. The increase in pressure rise due to a drop in annulus averaged static pressure at the inlet measurement location, which was taken to be just upstream of the inlet guide vanes as in the test compressor. When the inlet measurement plane is changed to the inlet of the computational domain, the pressure rise drops to a time average value of $\Psi(s-s) = 7.62$.

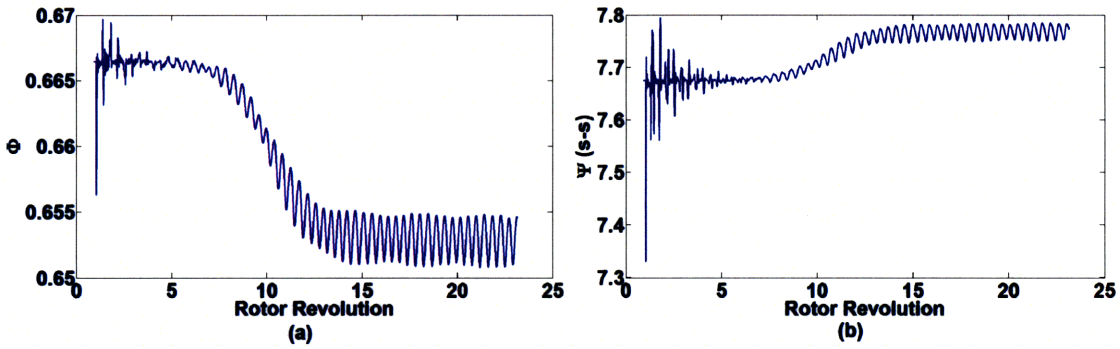

Figure 5-7: Time traces of $\Phi_{overall}$ and Ψ (s-s) for sensitivity Case 2 at $\Phi_{overall} = .691$

5.2.3 Case 3

Case 3 provided an intermediate test case with a slope in the body force curve from the peak pressure rise to zero flow between that of Case 1 and 3. The Φ_{local} traces for Case 3 at $\Phi_{overall} = .748$ are shown in Figure 5-8. The final flow pattern, shown in

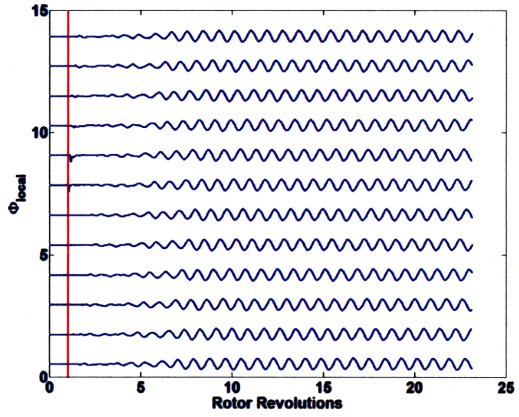

Figure 5-8: Traces of Φ_{local} for sensitivity Case 3 at $\Phi_{overall} = .748$ showing rotating modal stall pattern

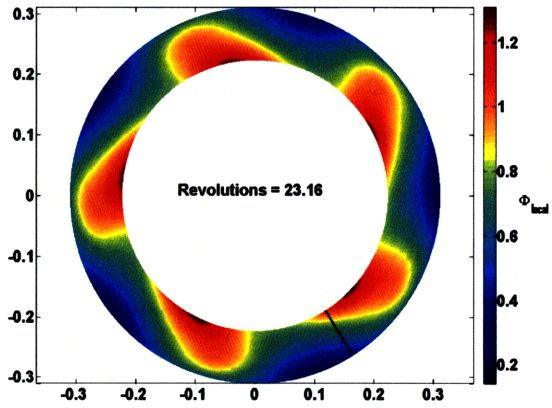

Figure 5-9: Pseudocolor plot of Φ_{local} for sensitivity Case 3 showing 5 lobed rotating stall pattern at $\Phi_{overall} = .748$

Figure 5-9, is characterized by a five lobed pattern of alternating high and low flow regions that rotate around the annulus at 23% rotor speed.

The Φ_{local} traces and lobed pattern resemble the flow patterns seen in Case 2, but with a drop in both Φ and Ψ (s-s).

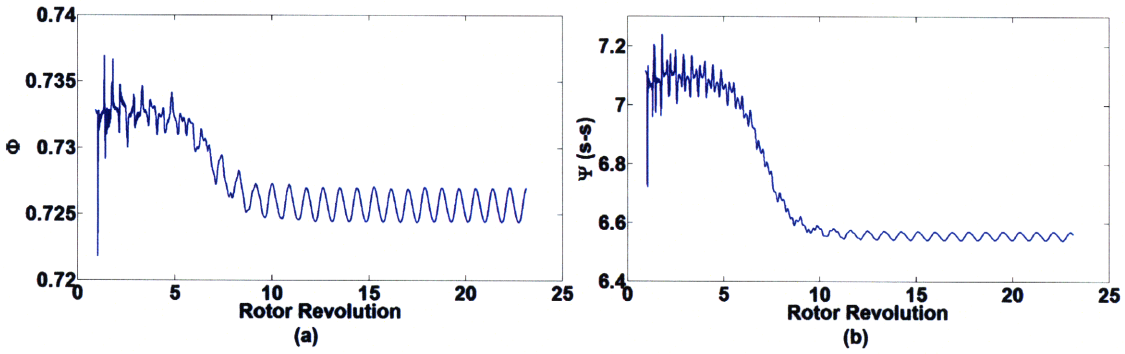

Figure 5-10: Time traces of $\Phi_{overall}$ and Ψ (s-s) for sensitivity Case 3 at $\Phi_{overall} = .748$. Both Ψ (s-s) and Φ level out to steady mean values by 20 rotor revolutions

5.2.4 Summary of Sensitivity Study of Shape of the Force Curve Near the Peak

The results of the study regarding the effects of changes to the force curves near the peak are summarized in Table 5.2. The data indicate the stall point estimate and inception type are sensitive to changes in the slope of the forces past the peak of the pressure rise.

The small amplitude of the final motion in Case 2 is not unexpected given the body force curves. Since $\frac{\Delta P}{\rho} \approx \int_{LE}^{TE} F_x dx$, a constant body force past the peak to zero flow implies a flat pressure rise curve below the flow coefficient corresponding to the peak.

Greitzer [1981] proposed an energy argument relating the slope of the pressure rise characteristic to the growth or decay of a disturbance. If a disturbance of $\delta\dot{m}$ and $\delta\Delta P$ is superimposed over the mean flow for an operating point on the negative slope of the characteristic, $\delta\dot{m}$ and $\delta\Delta P$ carry opposite signs. Their product, energy input

Case	Φ_{stall}	$\frac{\Phi_{stall}-\Phi_{stall,\,baseline}}{\Phi_{stall,\,baseline}} * 100$	Inception Type	Final Stall Type or Flow Pattern
1	.832	+24.2%	Spike	Part span rotating stall cell
2	No Stall	N/A	N/A	8 lobed pattern of high flow
3	.748	+11.6%	Unclear	5 lobed rotating stall pattern
Baseline	.670	0.0%	Spike	Ring stall

Table 5.2: List of cases for changing shape of force curve near peak

to the system, is negative and thus there is low energy input into the system and the perturbation decays. If the slope of the pressure rise curve is positive however, then the product of $\delta\dot{m}$ and $\delta\Delta P$ is positive and there is higher energy input than with a uniform flow, resulting in a disturbance that grows. Thus, if the slope of the pressure rise curve is negative *at all* operating points, a disturbance cannot grow at any operating point.

The body forces corresponding to Case 1 and the baseline differed only from $\Phi_{overall} = 0$ to $\Phi_{overall} = .78$, yet Case 1 exhibited stall at a flow coefficient 24% higher than the baseline. Case 1 also does not exhibit ring stall (as in the baseline), and the part span stall cell in Case 1 rotates at a slower speed than the stall cell in the baseline.

The results of Case 1 indicate that the stall inception estimate is sensitive to the slope of the body force curves near (and below) the peak. However the changes to the slope near the peak modify the forces from the peak to reverse flow. The sensitivity studies to follow will help to isolate the effects of changes to force curves near zero flow and in the reverse flow region.

5.3 Sensitivity to Force at Zero Flow

It is possible during stall that a local region of flow passes through zero flow conditions thus necessitating a $\Phi\Phi = 0$ data point on the force curve. There is little data on

the flow fields in this regime [1990], and two test cases were developed to assess the sensitivity of the stall simulation to the specification of forces here and at zero flow.

Each case utilized the full set of streamline curvature body forces from design to

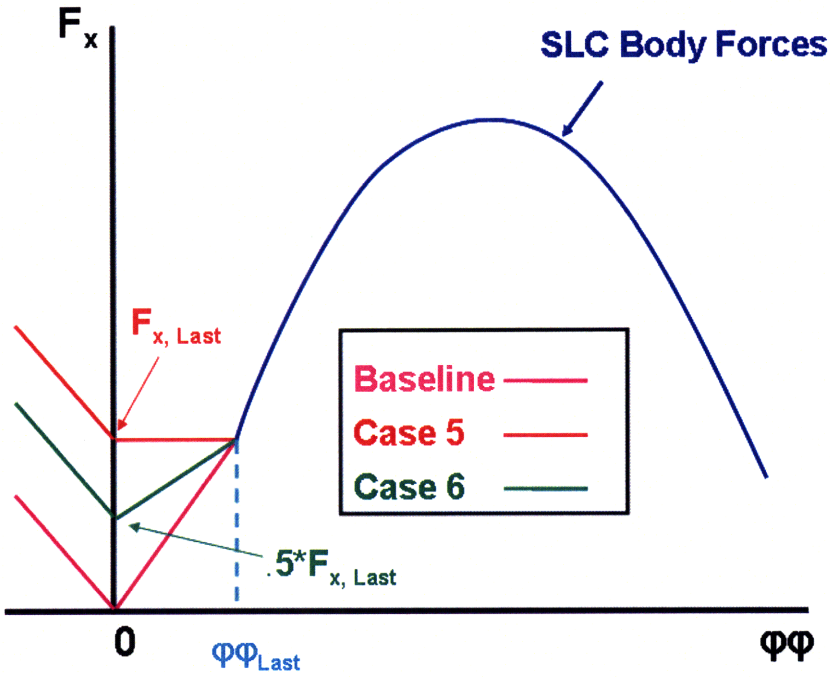

Figure 5-11: Graphical representation of force curves for zero flow force value sensitivity study

$\Phi_{overall} = .44$ but was joined to two different values of $F_{\Phi_{overall}=0}$.

The test cases are shown in Figure 5-11. The lines to zero flow were defined by F_{Last} (Case 5) and $\frac{F_{Last}}{2}$ (Case 6), where F_{Last} is the body force at $\Phi_{overall} = .44$. It was expected that changes in the zero flow force value would have less impact on the slope of the force curve near $\Phi_{overall} = .78$, thus isolating the effect of changing the force value at zero flow from changes to the curve near $\Phi_{overall} = .78$.

The pressure rise characteristics for Case 5 and Case 6 are plotted in Figure 5-12. The pressure rise curves for the cases only differ in the value of the lowest flow coefficient UnsComp is able to calculate an axisymmetric solution without reverse flow. This agreement of the pressure rise curves occurs because the body force curves are the same for flow coefficients above $\Phi_{overall} = .44$.

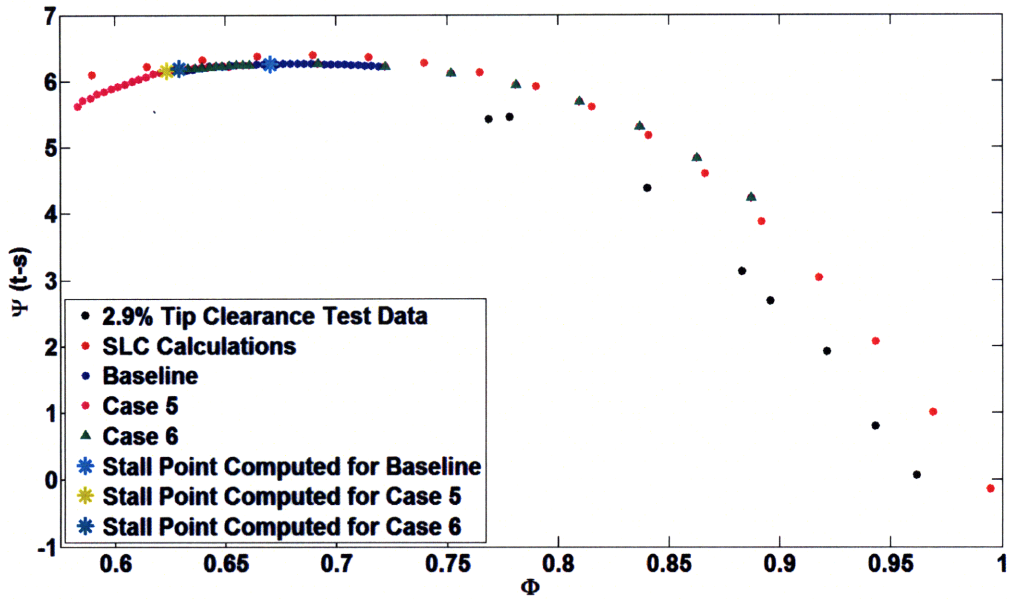

Figure 5-12: Total-to-static pressure rise curves for Cases 5 and 6

5.3.1 Case 5

Case 5 stalled through modal stall inception at $\Phi_{overall} = .624$ as in Figure 5-13 which plots the Φ_{local} traces at the rotor exit. The input spike initially rotates around

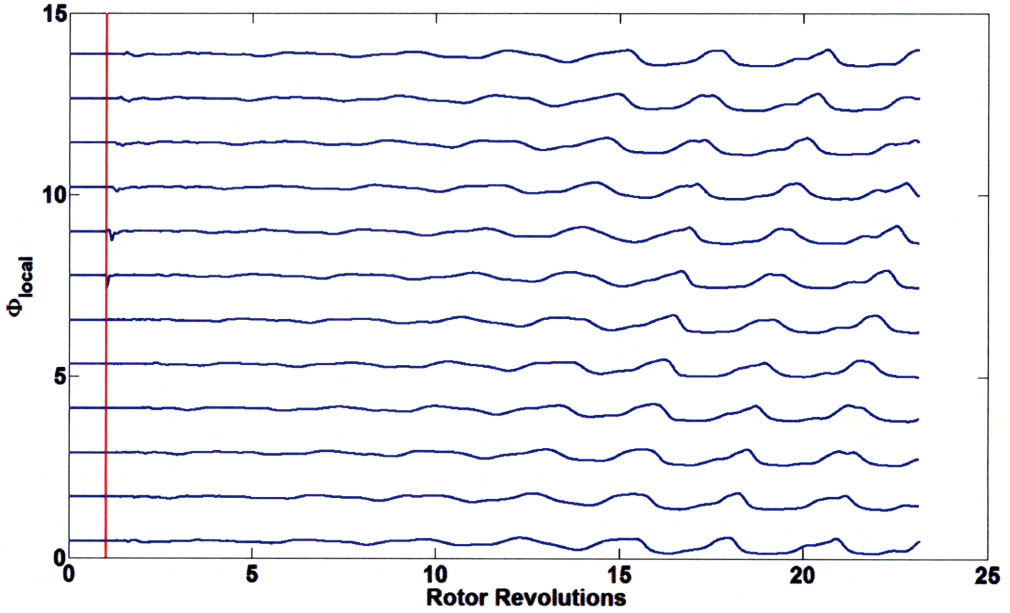

Figure 5-13: Traces of Φ_{local} for sensitivity Case 5 showing modal stall inception at $\Phi_{overall} = .624$ leading to part span rotating stall

the annulus at 67% rotor speed but disappears in less than one rotor revolution, at which point long wavelength oscillations characteristic of modal stall appear. After approximately nine rotor revolutions a part span stall cell is seen rotating around the annulus at 34% rotor speed. Figure 5-14 shows that the final form of stall was a part span rotating stall cell.

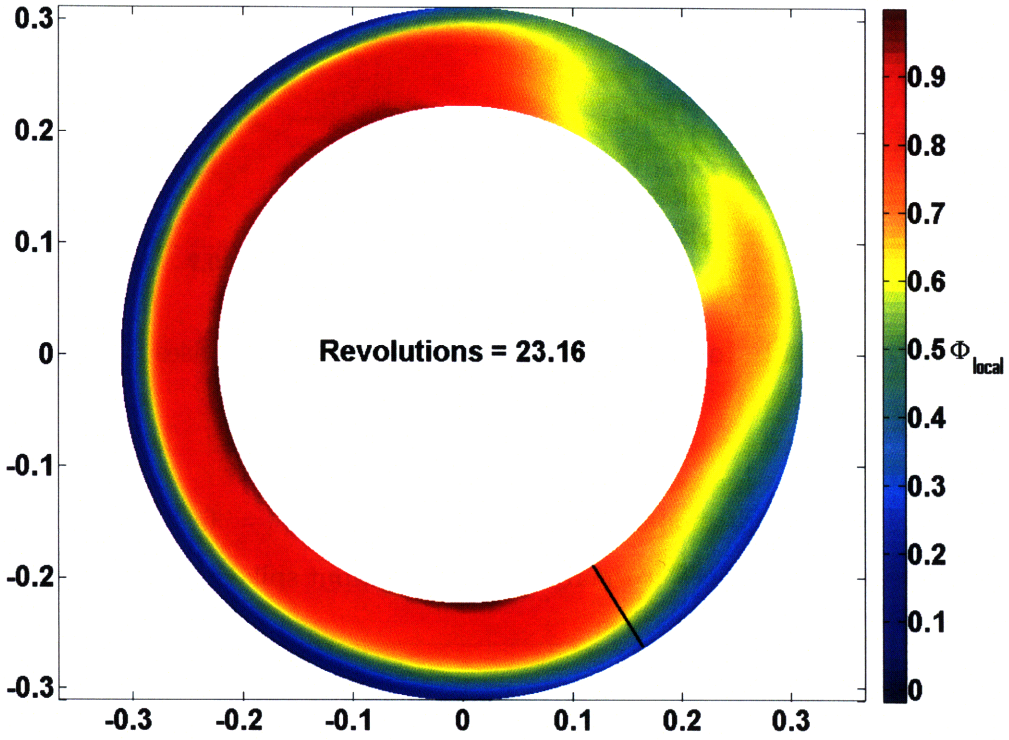

Figure 5-14: Pseudocolor plot of Φ_{local} for Case 5 showing rotating part span stall cell at $\Phi_{overall} = .624$

5.3.2 Case 6

Stall simulation results for Case 6 are given in Figure 5-15 which shows Φ_{local} traces at the rotor exit. The compressor appears to stall, at $\Phi_{overall} = .629$, through modal inception that grows into a rotating stall cell. Within one rotor revolution of appearing, the rotating stall cell encompasses the entire annulus leading to ring stall.

The cause of oscillations that appear at fifteen rotor revolutions is not yet known. In Figure 5-17 the annulus average values of $\Phi_{overall}$ and Ψ (s-s), show a drop in the pressure rise of the compressor after the input disturbance.

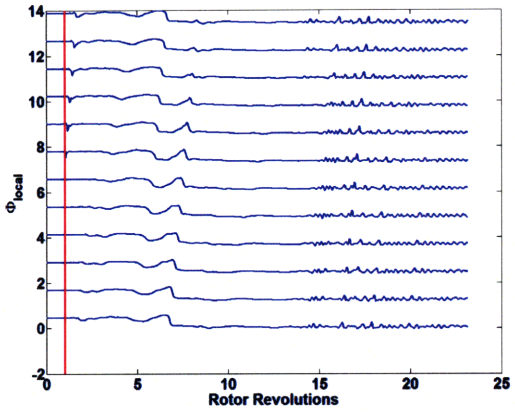

Figure 5-15: Traces of Φ_{local} for Case 6 showing modal stall inception at $\Phi_{overall} = .629$ leading to part span rotating stall

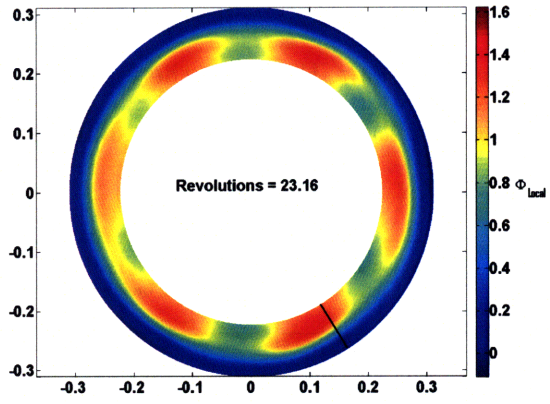

Figure 5-16: Pseudocolor plot of Φ_{local} for Case 6 showing rotating part span stall cell at $\Phi_{overall} = .629$

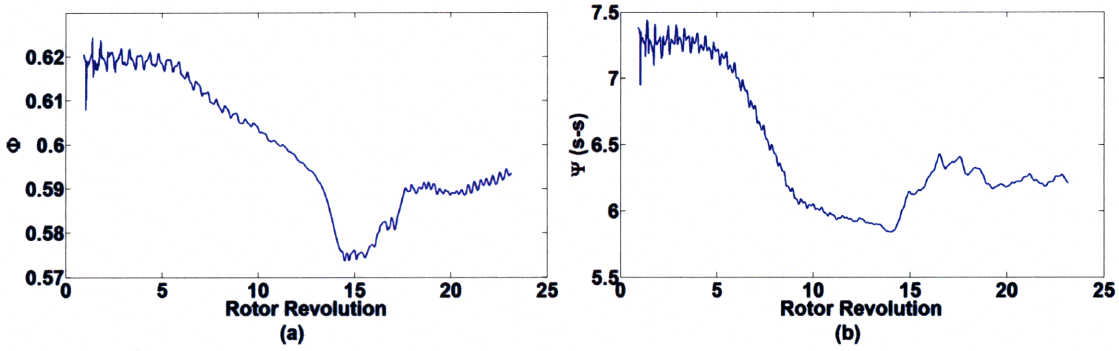

Figure 5-17: Time traces of $\Phi_{overall}$ and Ψ (s-s) for Case 6 at $\Phi_{overall} = .629$. Both Ψ (s-s) and Φ level out to steady mean values by the twentieth rotor revolution, indicating a limit cycle has been reached

5.3.3 Summary of Sensitivity to Value of Force at Zero Flow

The results of the sensitivity study into the effects of changing the force value at zero flow are listed in Table 5.3, including the baseline for reference.

Case 5 stalled at 7% lower flow coefficient than the baseline. There was modal type inception with the final form a part span stall cell. Case 6 had stall inceptoin at 6% lower flow coefficient than the case. There was a short lived modal inception pattern with the final form of ring stall, accompanied by small oscillations in the Φ_{local} traces near the end of the simulation.

The data indicates that the stall point estimate is not as sensitive to the force

value at zero flow as it is to the change in slope of the force curve between zero flow and the peak. However, the force input in the zero flow region does appear to change the inception pattern, reproducing spike type stall inception only when the force at zero flow was set to zero.

Case	Φ_{stall}	$\frac{\Phi_{stall}-\Phi_{stall,\,baseline}}{\Phi_{stall,\,baseline}} * 100$	Inception Type	Final Stall Type or Flow Pattern
Baseline	.670	0.0%	Spike	Ring stall
5	.624	-6.9%	Modal	Part span stall cell
6	.629	-6.1%	Modal (short)	Ring stall with oscillations

Table 5.3: Summary table of results from sensitivity analysis of changing force value at zero flow

The slope of the body force curve near zero flow can affect the stall inception type as follows. The force is related approximately to the local pressure rise by $\frac{\Delta P}{\rho} \approx \int_{LE}^{TE} F_x dx$. If during stall inception, a region of flow decelerates to low or reverse flow conditions, the slope of the body force curve in this regime could then determine the rate at which a disturbance grows or decays. The energy argument presented in Section 5.2.4, stated that negatively sloped pressure rise characteristics tend to stabilize disturbances, while positively sloped pressure rise characteristics have the opposite effect. Given that the force curves are *roughly* pressure rise curves for the local cell to which they are applied, a negatively sloped force curve would extract energy from the perturbation, while a positively sloped force curve would input energy into the perturbation. For a disturbance that sees many cells with steeply positive sloped force curves, the disturbance will grow rapidly, while shallower force curves lead to disturbances that grow at slower rates.

The baseline is characterized by a sharply positive force curve near zero flow, Case 5 has a zero slope force curve at zero. The simulations show that the baseline exhibits spike type stall inception, large amplitude, rapidly growing disturbances. Case 5 exhibits modal stall, which is characterized by long wavelength, small amplitude and slow moving disturbances.

5.4 Sensitivity to Slope of Reverse Flow Region of Force Curve

Stall cells are characterized by low or reverse flow conditions. Gamache and Greitzer [1990] showed that a compressor in reverse flow has a steeply negative pressure rise curve. For the baseline stall simulation a force per unit mass of $F_{x,reverse} = 7.6$ was input at $\Phi_{overall} = -.2$ which produces a steep negative slope in the force curve in the reverse flow region.

Case	$F_{\Phi_{overall}=-.2}$
7	$5 * F_{rev}$
8	$\frac{F_{rev}}{2}$

Table 5.4: List of cases for changing slope of force curve in reverse flow region

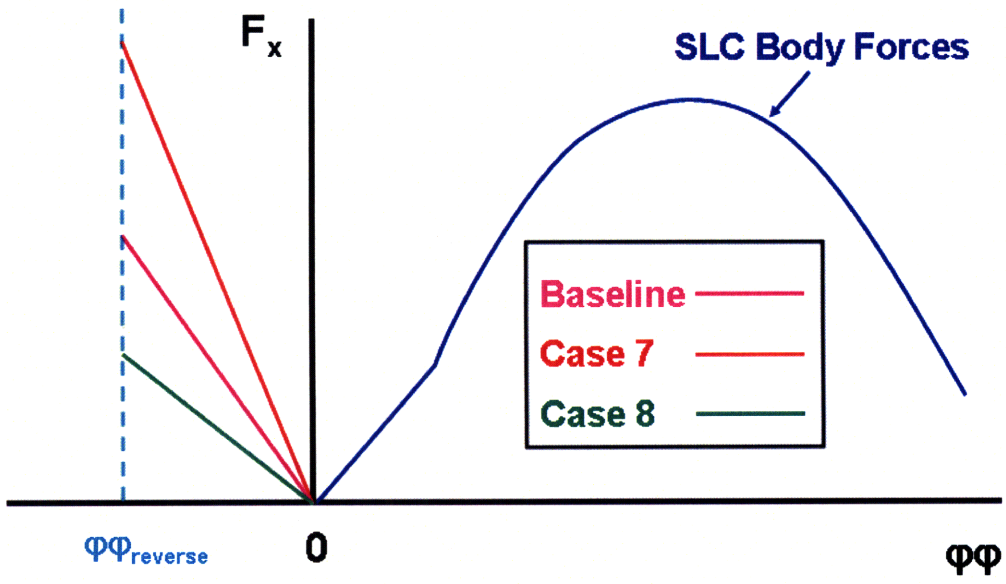

Figure 5-18: Graphical representation of force curves for reverse flow force value sensitivity study

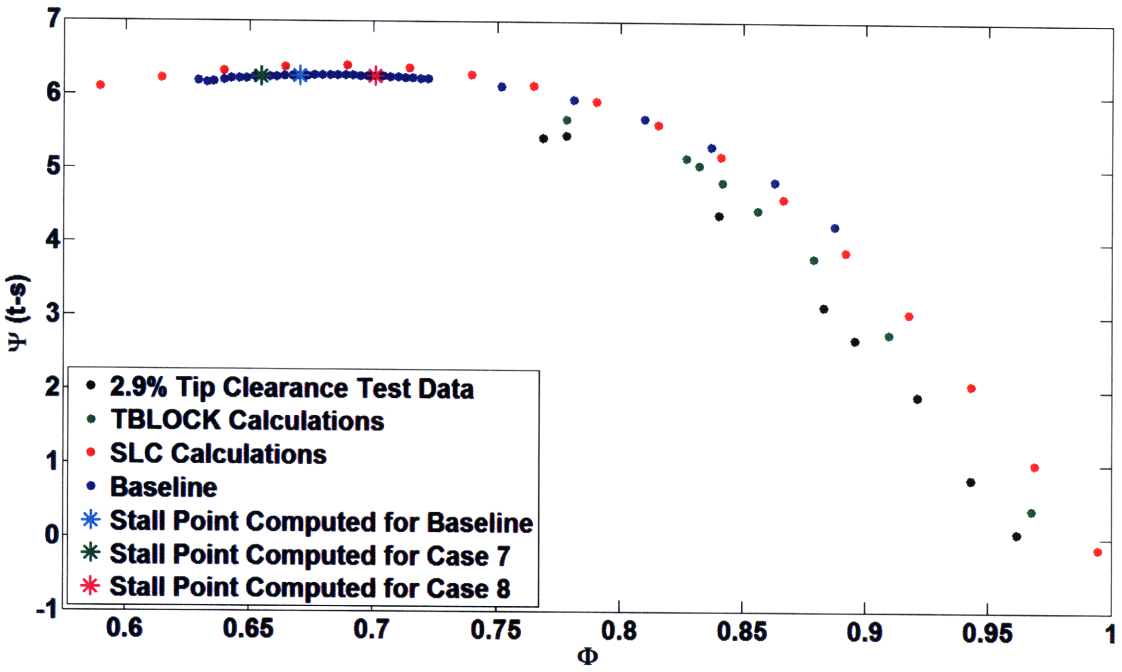

Figure 5-19: Total-to-static pressure rise curves for Cases 7 and 8

To test the sensitivity of the stall onset estimates to the slope of the reverse flow portion of the force curve, two test cases were compared to the baseline, as listed in Table 5.4. Figure 5-18 shows graphical representations of the test cases compared to the baseline. Case 7 had $F_{\Phi_{overall}=-.2} = 5 * F_{rev}$, a steeper slope than the baseline, while Case 8 had $F_{\Phi_{overall}=-.2} = \frac{F_{rev}}{2}$, resulting in a shallower slope than the baseline.

Figure 5-19 shows a plot of the pressure rise characteristic for the baseline with the stall points from Cases 7 and 8 included as cyan and yellow stars, respectively. The pressure rise curves for Cases 7 and 8 are the same as that for the baseline since all three cases share the same set of body forces from design to zero flow, and only vary for reverse flow. Since the axisymmetric pressure rise curves are only plotted up to the last stable operating point at which no reverse flow exists in the solution, the operating points are the same, to within computational error.

5.4.1 Case 7

Case 7 exhibited spike type stall inception at $\Phi_{overall} = .655$, leading to a part span rotating stall cell as seen in Figure 5-21. The input spike travels at 67% rotor speed

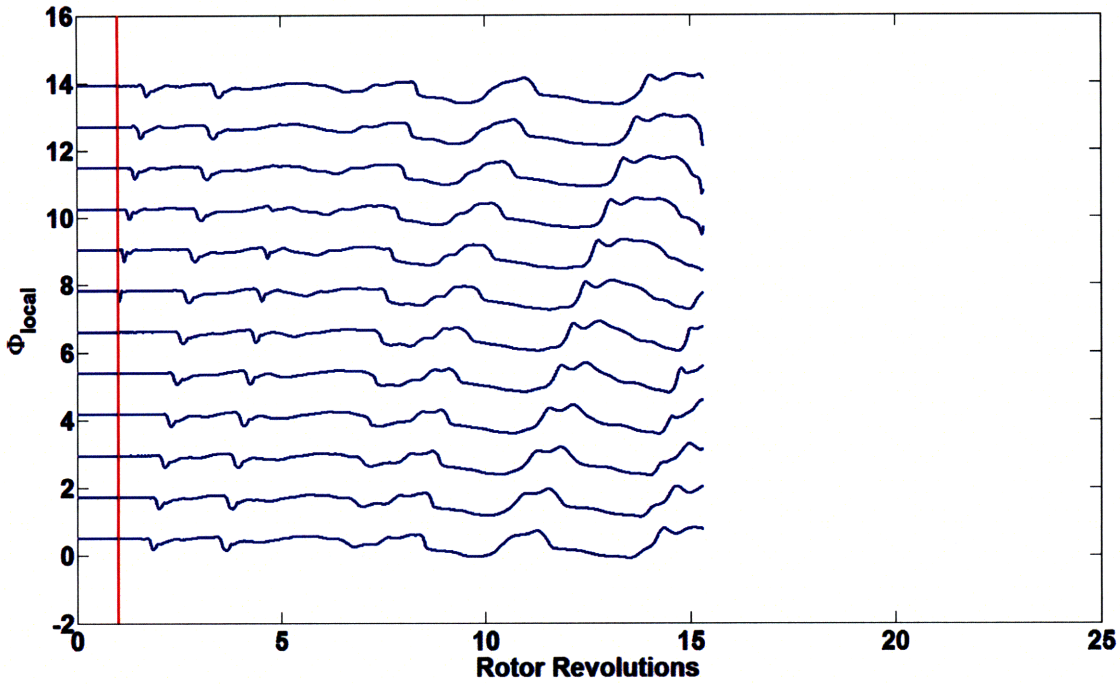

Figure 5-20: Traces of Φ_{local} for Case 7 showing spike type stall inception at $\Phi_{overall} = .655$ leading to part span rotating stall

and grows until roughly 4.5 rotor revolutions, after which it disappears for roughly one rotor revolution and then a part span rotating stall cell appears at about the sixth rotor revolution.

At approximately the fifteenth rotor revolution the computation encountered an

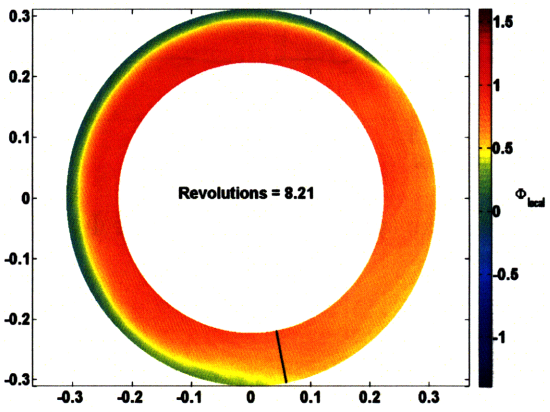

Figure 5-21: Pseudocolor plot of Φ_{local} for Case 7 showing part span rotating stall cell at $\Phi_{overall} = .655$

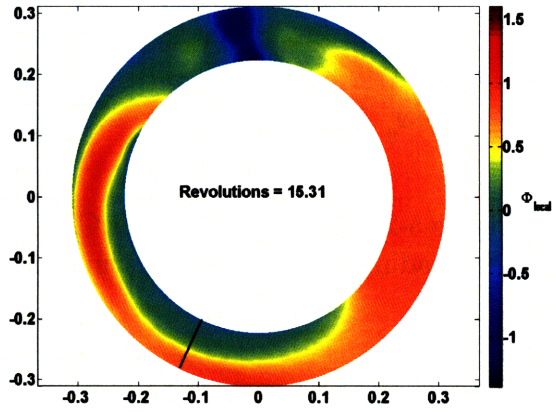

Figure 5-22: Pseudocolor plot of Φ_{local} for Case 7 showing reverse flow region extending from casing to hub just prior to crash of calculation

error. Just prior to the error, a column of reverse flow was observed extending from the casing to the hub, as seen in Figure 5-22, with the magnitude of the reverse flow velocity growing until the computation stopped. The cause of this error is not yet known.

5.4.2 Case 8

The Φ_{local} traces for Case 8 at $\Phi_{overall} = .701$ are shown in Figure 5-23. There is a spike input at one rotor revolution that rotates at 67% rotor speed. The spike grows into a part span rotating stall cell rotating at 50% rotor speed prior to developing into ring stall. Figure 5-24 shows a pseudocolor plot of the ring stall structure at the exit of the rotor at 23.16 rotor revolutions.

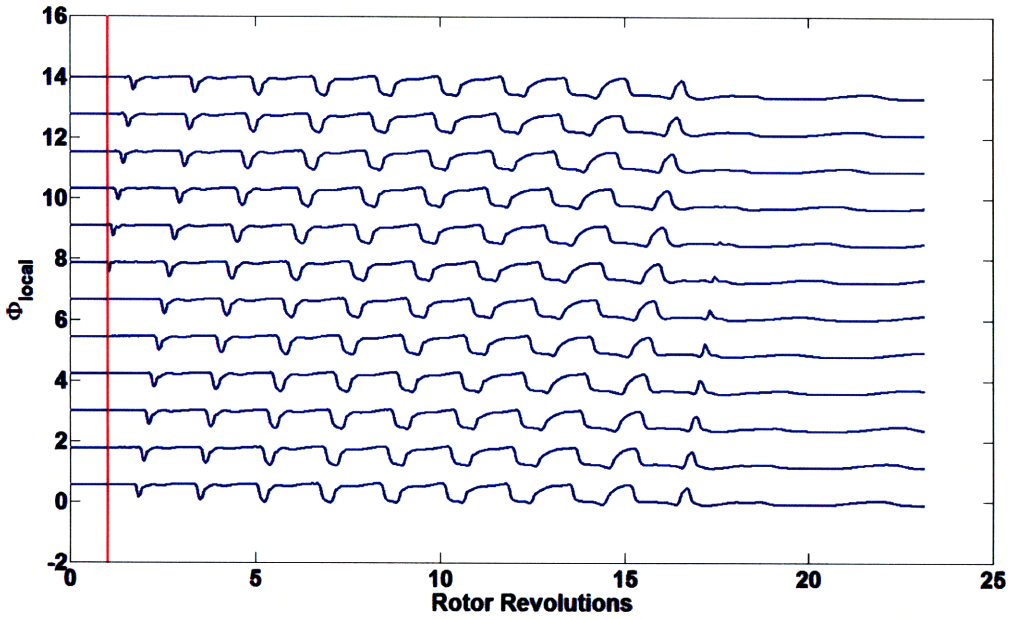

Figure 5-23: Traces of Φ_{local} for Case 8 showing spike type stall inception at $\Phi_{overall} = .701$ leading to part span rotating stall

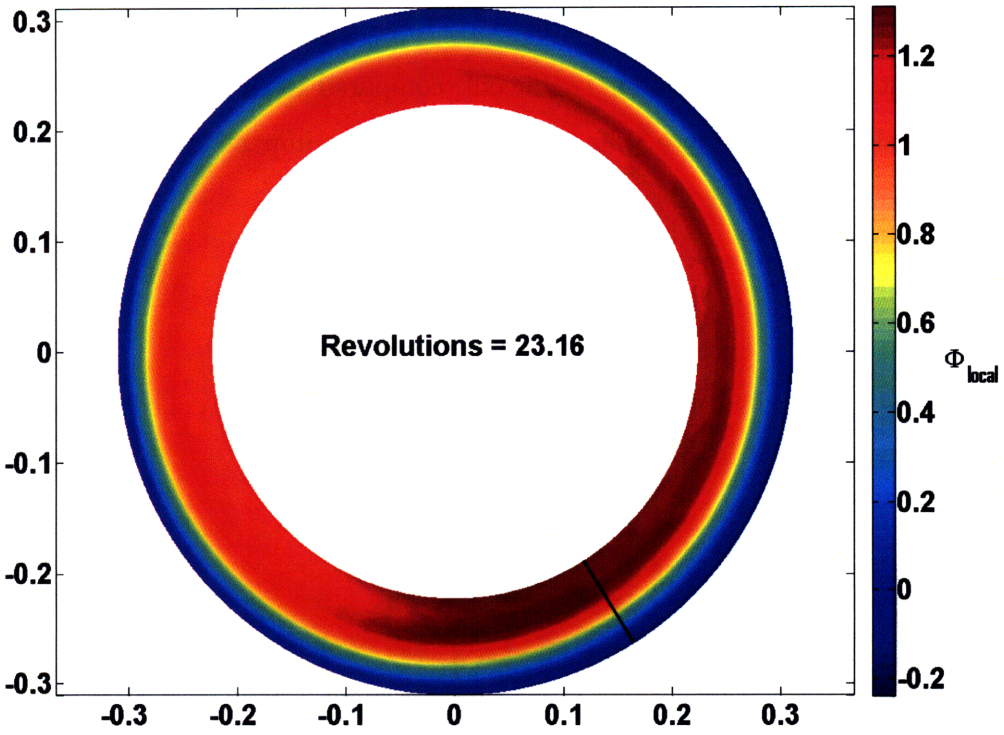

Figure 5-24: Pseudocolor plot of Φ_{local} for Case 8 showing part span rotating stall cell at $\Phi_{overall} = .701$

5.4.3 Summary of Sensitivity to Slope of Reverse Flow Region of Force Curve

Table 5.5 lists the results of the test cases used to assess the sensitivity to slope of the body force curve in the reverse flow region.

Case	Φ_{stall}	$\frac{\Phi_{stall} - \Phi_{stall,\,baseline}}{\Phi_{stall,\,baseline}} * 100$	Inception Type	Final Stall Type or Flow Pattern
Baseline	.670	0.0%	Spike	Ring stall
7	.655	-2.2%	Spike	Part span stall cell
8	.701	+4.6%	Spike	Ring stall

Table 5.5: Summary table of results from sensitivity analysis of changing force value at zero flow

Both Case 7 and 8 captured spike type stall inception, at flow coefficients within 5% of the baseline stalling flow coefficient. The final form of stall in Case 7 was a part span stall cell rather than the ring stall seen in the baseline and in Case 8. The

slope of the reverse flow portion of the body force characteristic thus does not have a significant effect on the stalling coefficient, compared to the slope of zero flow force value and slope of the curve near the peak, but does impact the final form of stall observed.

Chapter 6

Summary, Conclusion and Future Work

6.1 Summary of Work Presented

This thesis addresses the use of body forces from streamline curvature and from three-dimensional CFD computations.

Chapter 1 presented an overview of compressor stability with a focus on the two types of stall inception and a review of body force models for stability calculations.

Chapter 2 reviewed the requirements for a body force database and provided background on the CFD codes used to generate the body forces in this project, as well as their limitations.

Chapter 3 presented an analysis of the non-uniqueness observed in the Φ_{local} variable in the TBLOCK data set and proposed a fix for this limitation using the variable $\Phi_{local}|\Phi_{overall}|$. This enables use of the TBLOCK data in the UnsComp stability code.

Chapter 4 described a proposal, based on qualitative information about the stalled flow behavior, for joining the streamline curvature and TBLOCK body force databases.

Chapter 5 presented a set of sensitivity studies to determine the change in stall point and in type of stall that are associated with changes to the shape of the body force curves at flows below peak pressure rise flow coefficient. A stability analysis using streamline curvature body forces with changes to the shapes of the body force

curves past the peak highlighted areas of the body force curve and joining procedure that are important in determining stall point and inception type estimates.

6.2 Conclusions

1. The stall inception type was not sensitive to changes in the reverse flow body forces, but it was sensitive to the body forces at zero flow. The slope of the body force curve approaching zero flow from positive flow coefficients can thus be factor in determining the stall inception pattern.

2. The slope of the pressure rise curve near the peak has the largest effect on the stall point of all the parameters tested in this thesis. The maximum change seen in the stall point estimate over the cases examined was 24% and some cases failed to stall all together. The results are in agreement with the findings of Gong [2008].

3. Changes to the force value at zero flow provided an average of 6.5% change in stalling flow coefficient and changes to the reverse flow part of the force curves incurred less than 5% changes to the stalling flow coefficient.

4. The body force expressed as a function of the $\Phi\Phi$ reference variable can provide a means to adapt the TBLOCK data into a form suitable for use in the stability analysis code, UnsComp. There are 10% differences in the computed stall onset points between the procedures using the $\Phi\Phi$ reference variable and that using the Φ_{local} reference variable. However the $\Phi\Phi$ variable has the advantage of being applicable to both the TBLOCK and streamline curvature data sets.

5. Based on the results of the sensitivity study, the joining procedure proposed in this thesis should be assessed in terms of constraints on the slopes of the body force curves. In particular large changes in slope of the body force curves that arise as a result of the joining procedure.

6. The stall simulation results with the streamline curvature body forces have allowed assessment of the effects of the body force representation on stall onset and pattern. While the impetus for using the TBLOCK body forces was to include the effects of tip clearances, once can also to model tip clearance effects in a streamline

curvature framework. In view of the goal of providing a simple yet accurate stall estimation tool, it might be useful to consider the idea of incorporating tip clearance effects into a streamline curvature simulation and body force computation.

6.3 Proposed Future Work

1. The changes to the body force curves used in this thesis were coupled in that changes to the slope of the body force curves near the peak changed the slope of the body force curve and the force value near zero flow at that point. A sensitivity analysis on the effect of the slope of the body force curve near the peak, but with a constant slope curve in the low flow region of the body force curve should be performed to isolate the effects of the slope changes near zero flow and those near the peak.

2. The TBLOCK body forces provide body forces that are more accurate representation of the body forces within the actual compressor and also include the effects of tip clearances. However, the grid currently used in the stall simulation smears out the tip gap, in the radial direction, into one cell within UnsComp. The effects of radial grid size should be investigated.

3. Initial stall simulations using the TBLOCK body forces did not yield disturbances that grew into a stall cell. The computed pressure rise across the rotor was lower than the pressure rise across the stator with the TBLOCK body forces. The streamline curvature body forces, which reproduce spike type stall inception, as in the data, exhibit a higher pressure rise across the rotor than that across the stator. An investigation of the cause of the discrepancy in the computed pressure rises should be carried out.

4. The procedure for joining the TBLOCK and streamline curvature body forces presented in this thesis uses the TBLOCK body forces up to the last available flow coefficient and then extends curves from this point to low and reverse flow. A sensitivity study similar to the one performed in this thesis, but using TBLOCK body forces, should be carried out. This study would be a generalization of the proposed joining procedure that joined a simple set of curves to the fixed TBLOCK body forces.

5. When using the $\Phi\Phi$ reference variable in conjunction with the streamline curvature body forces, UnsComp simulated the compressors final stall state to be ring stall. However when the original Φ_{local} reference variable is used the compressor does not exhibit ring stall. A simulation should be run using the streamline curvature body forces and the Φ_{local} variable, for longer (50 rotor revolutions to determine if the compressor is prone to ring stall or if the ring stall is an effect of the use of the $\Phi\Phi$ variable.

6. While stability calculations using the $\Phi\Phi$ reference variable estimate stall to within 8% of the measured value and correctly simulate the spike type stall inception seen in the test compressor, there is not a rigorous justification for the $\Phi\Phi$ variable. The variable provides a reduction in the number of double values in TBLOCK and allows for their incorporation into the simulation, but a reference variable which is a function of two local flow quanities may be better suited to the robsustness of the overall procedure.

Appendix A

Body Force Description and Equations

A.1 Governing Equations

The incompressible form of the Navier-Stokes equations in cylindrical form are given by Greitzer, Tan and Graf [2004] as:

$$\frac{1}{r}\frac{\partial V_r^2 r}{\partial r} + \frac{1}{r}\frac{\partial V_r V_\theta}{\partial \theta} + \frac{\partial V_r V_x}{\partial x} + \frac{V_\theta^2}{r} = -\frac{1}{\rho}\frac{\partial P}{\partial r} + \hat{r}\cdot\nabla\underline{\underline{\tau}} + \frac{\Omega V_\theta}{r} + \frac{\Omega^2}{r^2} + F_r \tag{A.1}$$

$$\frac{1}{r}\frac{\partial V_r V_\theta r}{\partial r} + \frac{1}{r}\frac{\partial V_\theta^2}{\partial \theta} + \frac{\partial V_x V_\theta}{\partial x} + \frac{V_x V_\theta}{r} = -\frac{1}{r\rho}\frac{\partial P}{\partial \theta} + \hat{\theta}\cdot\nabla\underline{\underline{\tau}} - \frac{\Omega V_r}{r} + F_\theta \tag{A.2}$$

$$\frac{1}{r}\frac{\partial V_r V_x r}{\partial r} + \frac{1}{r}\frac{\partial V_\theta V_x}{\partial \theta} + \frac{\partial V_x^2}{\partial x} = -\frac{1}{\rho}\frac{\partial P}{\partial x} + \hat{x}\cdot\nabla\underline{\underline{\tau}} + F_x \tag{A.3}$$

The variables $\hat{x}$, $\hat{\theta}$, and $\hat{r}$ represent unit vectors in the axial, tangential and radial directions, respectively, while $\underline{\underline{\tau}}$ is the stress tensor.

A.2 Flux Form of Equations

The body force formulation relies on a flux form of the Navier Stokes equations. Specifically a conservative form of the Equations A.1 - A.2 as given by Equation A.4,

where $\mathbf{F}$, $\mathbf{G}$, $\mathbf{H}$ and $\mathbf{S}$ are given by:

$$\mathbf{F} = \begin{bmatrix} r\rho V_x \\ r\rho V_x^2 + rP \\ r\rho V_x r V_\theta \\ r\rho V_x V_r \end{bmatrix} b \ , \ \mathbf{G} = \begin{bmatrix} r\rho V_\theta \\ r\rho V_x V_\theta \\ r\rho V_\theta^2 + rP \\ r\rho V_r V_\theta \end{bmatrix} b \ , \ \mathbf{H} = \begin{bmatrix} r\rho V_r \\ r\rho V_x V_r \\ r\rho V_r r V_\theta \\ r\rho V_r^2 + rP \end{bmatrix} b$$

$$\mathbf{S} = \begin{bmatrix} 0 \\ br\rho F_x + rP\frac{\partial b}{\partial x} \\ br\rho r F_\theta + rP\frac{\partial b}{\partial \theta} \\ b\rho V_\theta^2 + bP + br\rho F_r + rP\frac{\partial b}{\partial r} \end{bmatrix}$$

$$\frac{\partial \mathbf{F}}{\partial x} + \frac{\partial \mathbf{G}}{\partial \theta} + \frac{\partial \mathbf{H}}{\partial r} = \mathbf{S} \tag{A.4}$$

Bibliography

[1998] Camp, T.R. and Day, I.J., 1998. "A Study of Spike And Modal Stall Phenomena in a Low-Speed Axial Compressor" *Journal of Turbomachinery* Vol. 120, pp.393-401

[2001] Choi, T.J., 2001. "Development of an Effective Computational Methodology for Multi-State Compressor Map Generation" Masters Thesis, Massachusetts Institute of Technology, Dept. of Aeronautics and Astronautics

[2004] Cumpsty, N.A., 2004. Aerodynamics Longman Publishing Group

[1993] Day, I.J., 1993. "Stall Inception in Axial Flow Compressors" *ASME Journal of Turbomachinery* Vol. 115, pp.1-9

[2007] Denton, J.D. Personal communication, 2007

[1990] Gamache, R.N. and Greitzer, E.M., 1990. "Reverse Flow in Multistage Axial Compressors" *Journal of Propulsion* Vol. 6, pp.461-473

[1999] Gong, Y., 1999. "A Computation Model for Rotating Stall and Inlet Distortions in Multistage Compressors" PhD Dissertation, Massachusetts Institute of Technology, Dept. of Aeronautics and Astronautics

[2008] Gong, Y., 2008. Personal Communication

[1981] Greitzer, E.M, 1981. "The Stability of Pumping Systems – The 1980 Freeman Scholar Lecture" Journal of Fluids Engineering, Vol 103, pp. 193-242

[2004] Greitzer, E.M., Tan, C.S., and Graf, M., 2004. *Internal Flow Concepts and Applications* Cambridge University Press

[1992] Kerrebrock, J. L., 1992. *Aircraft Engines and Gas Turbines* The MIT Press

[2008] Kiwada, G., 2008. "Development of a Body Force Description for Compressor Stability Assessment" Master's thesis, Massachusetts Institute of Technology, Dept. of Aeronautics and Astronautics

[2007] Longley, J.P., 2007. "Calculating Stall and Surge Transients" ASME Paper GT2007-27378

[1997] Longley, J.P., 1997. "Calculating the Flow Field Behavior of High-Speed Multi-stage Compressors" ASME Paper 97-GT-468

[1969] Reid, C., 1969. "The Response of Axial Flow Compressors to Intake Flow Distortion" ASME paper 69-GT-29

[1989] Steenken, W.G., 1989. "Engine Operability" in *Aircraft Propulsion Systems Design and Technology*, edited by G.C. Oates, American Institute of Aeronautics and Astronautics

[2009] Walker, T.K., 2009. "'The Development and Requirements of a Body Force Database from Two-Dimensional and Streamline Curvature Calculations" Masters Thesis, Massachusetts Institute of Technology, Dept. of Aeronautics and Astronautics

[2003] Xu, L., Hynes, T.P., and Denton, J.D., 2003. "Towards Long Length Scale Unsteady Modeling in Turbomachines" *Proc. Instm Mech. Engrs* Vol. 217 Part A: J. Power and Energy, pp. 75-82